Internal Report
H1 - 10/94 - 381
PRC 94/03
October 1994

Proposal for a Forward Proton Spectrometer for H1

by

Inter-University ULB-VUB, Brussels
DESY Hamburg
University Hamburg II. Institut f. Experimentalphysik
University Kiel
School of Physics and Materials, University Lancaster
Lebedev Physics Institute Moscow
INFN Roma Dipartimento di Fisica, La Sapienza Roma
DESY Institut f. Hochenergiephysik Zeuthen

"Die Verantwortung für den Inhalt dieses
Internen Berichtes liegt ausschließlich beim Verfasser"

H1 - 10/94 - 381
PRC 94/03

Proposal for a Forward Proton Spectrometer for H1.

Inter-University ULB-VUB, Brussels
DESY Hamburg
University Hamburg II Institut f. Experimentalphysik
University Kiel
School of Physics and Materials, University Lancaster
Lebedev Physics Institut Moscow
INFN Roma Dipartemento di Fisica, La Sapienza Roma
DESY Institut f. Hochenergiephysik Zeuthen

October 1st 1994

Abstract

It is proposed to upgrade the H1 detector by the addition of a forward proton spectrometer. This addition will enlarge the physics capability of H1 in studying diffractive processes. It is proposed to employ the Roman Pot technique and to build two stations at 81 and 90 m downstream the interaction point. The detectors inside the plunger vessels will be scintillating fiber hodoscopes with multi pixel photomultiplier read out sandwiched between trigger counters. The time schedule calls for installation into HERA during the shut down 1994 / 1995.

Contents

1 Introduction.

Deep inelastic high energy e - p interactions (DIS) predominantly proceed by the exchange of a virtual vector boson (γ, W or Z^o) between the incident electron and a constituent quark or gluon in the proton. The rest of the proton is essentially unaffected by the interaction and continues along the flight path of the incoming proton. In about one quarter of the neutral - and charged current deep inelastic interactions the proton remnants fragment into final states containing an energetic forward going proton at forward angles. In general these leading protons escape through the beam pipe and are not detected in the central HERA detectors. With the help of a Forward Proton Spectrometer (FPS) they can be recorded and their energy be measured. Further kinematical constraints could thus be applied and additional information on deep inelastic scattering final states will be gained. Two Feynman diagrams contributing to DIS processes are shown in Fig. 1.

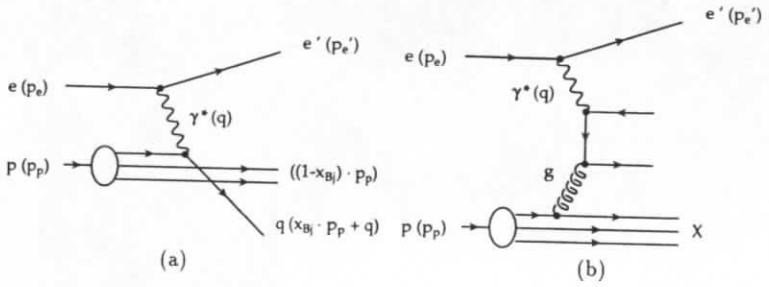

Figure 1: *Feynman diagrams describing deep inelastic electron scattering processes. a) scattering off a constituent quark, b) photon gluon fusion.*

In hadron hadron scattering a class of reactions is observed, which is characterised by low multiplicity and energetic forward going particles. These diffractive processes are attributed to the exchange of a Regge particle with vacuum quantum numbers, the Pomeron. Also in deep inelastic electron proton scattering reactions are observed which have all features of diffraction scattering. They have a small number of isolated forward going particles or in some cases only one energetic proton emitted at small angle of the order of 1 mrad. The rest of the final state particles are observed in the central rapidity region leaving a gap in rapidity space towards the forward going proton or proton debris which is free of particles. These rapidity gap events in deep inelastic scattering are interpreted by the exchange of a colourless object, a meson or a Pomeron. At HERA about 5 % of all DIS events above $Q^2 = 4$ GeV^2 are rapidity gap events with the gap extending to a pseudorapidity of $\eta = 1.8$ [1]. In diffractive DIS reactions the virtual photon scatters thus off a Pomeron, which is emitted by the target proton as sketched in Fig. 2.

Diffractive processes have been extensively studied in hadronic interactions in particular during the seventies and early eighties [2], where the phenomenology of the Pomeron exchange was analysed in terms of Regge models. The new input to complement the Regge picture is a QCD description of the Pomeron, in which it is assumed to be a condensate of quarks and gluons like ordinary hadrons or the photon. In DIS reactions the virtual photon is scattered off the Pomeron constituents and thus the study of deep inelastic diffractive processes allows an investigation into the Pomeron structure [3]. As shown in Fig. 3 the virtual photon may

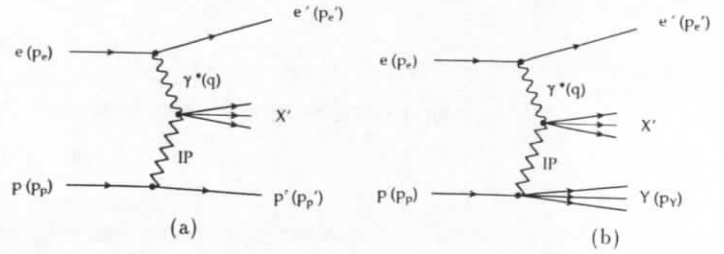

Figure 2: *Deep inelastic diffractive processes. a) elastic b) diffraction dissociation of the proton.*

couple to the gluonic or quark content of the Pomeron.

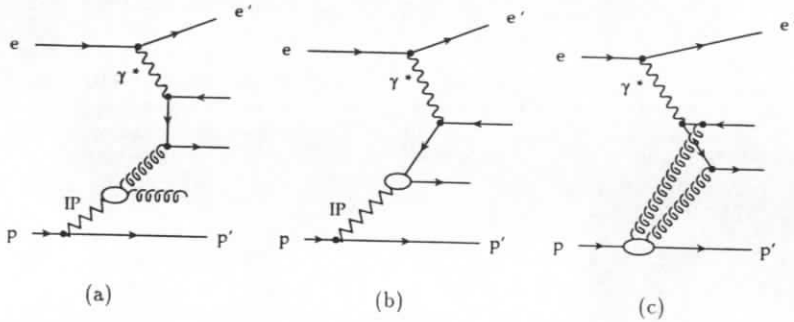

Figure 3: *a) and b) gluonic and quark content with Pomeron remnant, c)gluonic content without Pomeron remnant.*

In order to assure scattering off a Pomeron the target proton has to remain intact loosing only a small amount of energy. According to the diagrams of Fig.4 pion exchange may lead to final state configurations which are similar to those appearing in diffractive Pomeron exchange processes. Thus recording a forward going proton will not be sufficient to guarantee Pomeron exchange. The momentum of the forward going proton has to be measured as well, because according to the differential cross sections displayed in Fig. 5 the diffractive contribution may be considerably enhanced by restricting to a kinematic range, where the mass of the hadronic final state is small and the momentum fraction ν carried by the exchange particle does not exceed 10% of the incident proton's momentum. Stated in a different way these reactions are characterised by forward going protons which carry more than 90% of the beam energy and therefore in order to apply this cut the momentum of the scattered proton has to be known.

At HERA in deep inelastic diffraction scattering the Pomeron momentum is inferred from the measured momentum of the scattered proton and the virtuality of the incoming photon from the momentum of the scattered electron.

To get access to these processes we propose for H1 a forward spectrometer using the Roman Pot technique as already applied by the ZEUS collaboration [6]. The possibility to measure the Pomeron structure function in deep inelastic electron scattering has been studied in more detail [4] with the help of the POMPYT Monte Carlo program [5]. For these studies the nomenclature

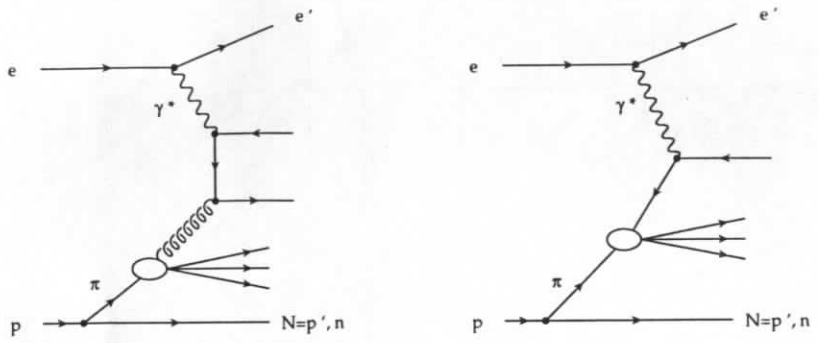

Figure 4: Pion exchange diagrams contributing to DIS processes.

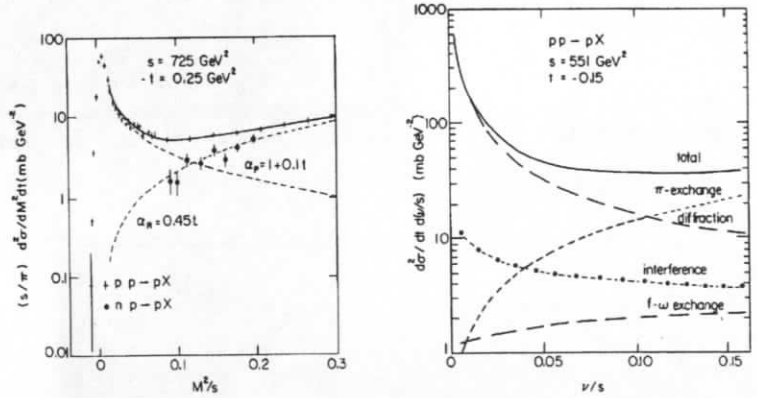

Figure 5: *Pion and Pomeron exchange contributions to proton nucleon scattering as function of the normalised mass of the final state system and the square of the fractional energy of the exchange particle.*

of Fig.2 will be used with $x_p = E'_p/E_p$, the fractional energy of the final state proton, $x_{Pom} = 1 - x_p$, the normalised Pomeron energy and $t = (p - p')^2$, the invariant momentum transfer to the proton squared. The maximum rapidity observed in an event will be denoted by η_{max}.
H1 and ZEUS have so far studied diffractive events by demanding no particles to be observed above a maximum rapidity η_{max} with typical values of $\eta_{max} \approx 1.8$. This requirement cuts severely into the kinematics of the reaction. The final state hadronic mass, the fractional momentum carried by the Pomeron, $x_{Pom} = 1 - x_p$ is most affected. Therefore replacing the rapidity cut by the observation of a forward proton will remove most of the kinematic constraints.
The new kinematic regime which will become accessible with a forward spectrometer consisting of two detector stations, at 81 and 90 m is discussed by referring to Figs. 6 and 7. In Fig. 6 events have been generated with the POMPYT event generator, which fulfilled the requirement that a rapidity gap exists between the forward going proton and a maximum rapidity $\eta_{max} = 1.8$. These events were then tracked through the H1 detector, where due to detector smearing some events appear at larger values of the rapidity variable than on the generator level. The figure clearly shows that a rapidity cut of 1.8 limits the value of the normalised Pomeron energy x_{Pom} to values below 10^{-2}. Values of x_{Pom} up to 10^{-1} become accessible if a forward going proton is required which passes through the two stations at 81 and 90 m as shown in Figure 7.

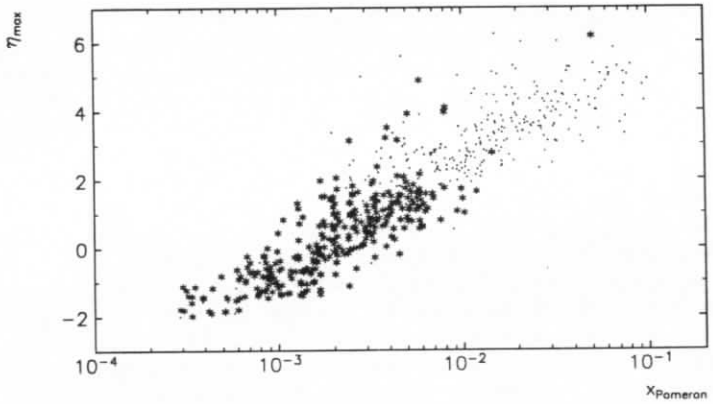

Figure 6: *The generated rapidity of the most forward going particle vs. the normalised Pomeron energy x_{Pom}. All events are tracked through H1.* * *denotes events generated with $\eta_{max} \leq$ 1.8, while · denotes all events (without η_{max} cut)*

Another process of typical diffractive nature is the photoproduction of vector mesons produced elastically or inelastically. In cases where only the proton is excited to a low mass state, elastic and inelastic channels are difficult to distinguish experimentally, because the scattered proton and the fragments from the decay of low mass excited states are in general not visible in the main detector. In previous experiments only global corrections have been applied based on model dependent Monte Carlo estimates. Here a forward proton spectrometer offers the possibility to record the scattered proton, separate the elastic and inelastic contributions on an event to event basis and identify Pomeron exchange processes.

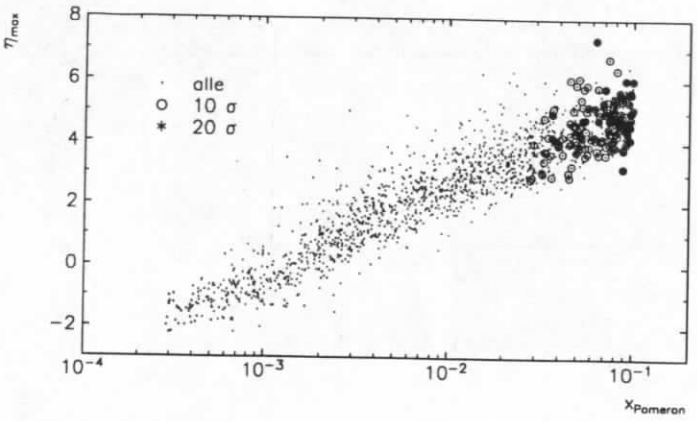

Figure 7: η_{max} *vs. the normalised Pomeron energy* x_{Pom}. *Circles and stars refer to events with forward protons which are detected at distances from the closed orbit of 10 and 20* σ *respectively in both stations at 81 and 90 m.*

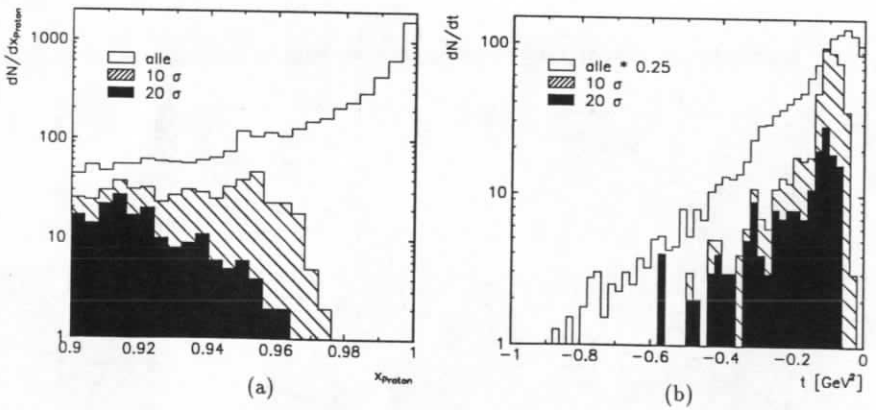

Figure 8: *a)*x_{Pom} *and b) t for events with protons traversing both detectors at 81 and 90 m. The acceptance is given for two different settings of 10* σ *and 20*σ *vertical distance from the closed orbit.*

The technique to record and momentum analyse leading protons with the help of the magnetic elements of the accelerator has been developed at the CERN ISR and SPS. Roman Pots (the first device has been built by a group from the Sanita Institut in Rome for the ISR), are movable vacuum inserts to house detector elements at atmospheric pressure. A plunger vessel can be brought close to the circulating beams to record particles with small deviations from the closed orbit. By installing several pots into the HERA machine, a forward spectrometer can be built in which trajectories for off – momentum particles are sampled at various points. Because of geometrical constraints imposed by the HERA machine components there is a maximum number of five positions where Roman Pots can be installed. Due to financial limitations it is proposed to install in a first stage only two stations located at distances of 81 and 90 meters downstream of the H1 interaction point.

The energy resolution of the forward spectrometer must be such that processes with Pomeron exchange can be separated from processes, where ordinary Regge trajectories are exchanged. Thus the minimum requirement is a momentum resolution, which enables us to tag events, where the scattered proton carries 90% or more of the beam momentum. Depending on the sharpness of this cut a 1% momentum resolution seems to be adequate. Another argument for defining the momentum resolution can be deduced from the requirement that the Pomeron structure function should be measured in at least three bins in x_P which also leads to a resolution of the order of 1%. This value is about one order of magnitude above the energy width of the circulating proton beam so that smearing effects due to the natural beam energy spread can safely be neglected. According to the properties of the magnetic channel this can be achieved with a spatial detector resolution of 100 μm taking into account additional uncertainties due to alignment errors and vertex smearing.

The necessary spatial resolution and the required radiation hardness of detectors, which are operated close to the circulating beam will determine the type of detector to be installed in the Roman Pots. We propose to employ scintillating fiber hodoscopes which have the additional advantage of being fast so that first level trigger signals can be formed.

The acceptance of such a Roman Pot spectrometer depends on the closest distance of approach of the detector elements to the circulating proton beam. Due to collimator settings in the HERA machine distances between 10 and 20 σ from the design orbit are possible corresponding to spatial separations between 2.3 and 4.6 mm. With these settings the acceptance of the spectrometer is of the order of 10% for diffractive events as deduced from Figure 8. More details on the beam profiles and acceptance calculations can be found in chapter 3.

2 Proton Spectrometer Beamline

The HERA machine elements between the H1 interaction point and the Roman Pot position at around 90 m downstream constitute a magnetic channel with quadrupoles and dipoles, which acts as a spectrometer for particles emerging from the interaction point.

The forward beamline is sketched in Fig.9 with the horizontal bending magnets BH04, the vertical bending magnets BU05 and the quadrupoles QS10 and QR14. The dispersion of the beamline spectrometer may be inferred from Fig. 10 with trajectories between 820 and 600 GeV.

By measuring the deviation of the particle trajectory from the closed orbit, one can thus determine scattered proton momenta. Intrinsic in this trajectory measurement is knowledge of the production vertex. Particles measured in the central H1 detector will be used for the determination of the latter. The absence of a production vertex leads to unconstrained conditions which render the proton momenta largely indeterminate.

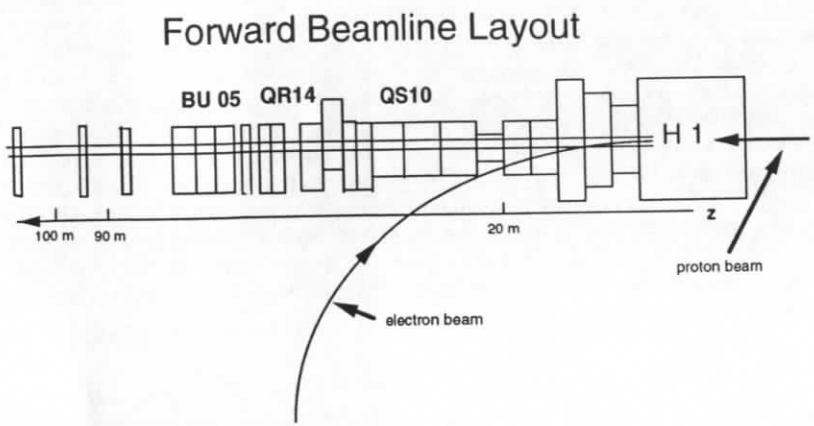

Figure 9: Forward Proton Beam Elements

2.1 Simulation of Trajectories

The proton trajectories can be simulated in various ways. In what follows, we describe two independent ways of trajectory simulation followed by a comparison of the two methods.

2.1.1 Simulation by GEANT

With the help of the GEANT simulation package the trajectory of protons in well-mapped magnetic fields traversing given volumes and material media can be simulated step-wise[7]. As a database we use the different volumes and magnetic field characteristics of the forward beam line elements from the interaction vertex downstream to 100 meters. For the magnetic field description we use the dipole field strengths B_x, B_y and for the quadrupole fields we introduce the field gradient.

2.1.2 Simulation by Transport Matrix Building

In contrast to the GEANT simulation, we can also proceed to represent each magnetic element by a transfer matrix and do the tracking by applying the appropriate transfer matrices for quadrupoles and dipoles with magnetic field strengths copied from the HERA optics settings. Both methods give results, which agree within about 1%. The computing time to track particles is shorter for the matrix method, while a GEANT calculation is more flexible and provides easy access to the particle coordinates at various points along the beamline.

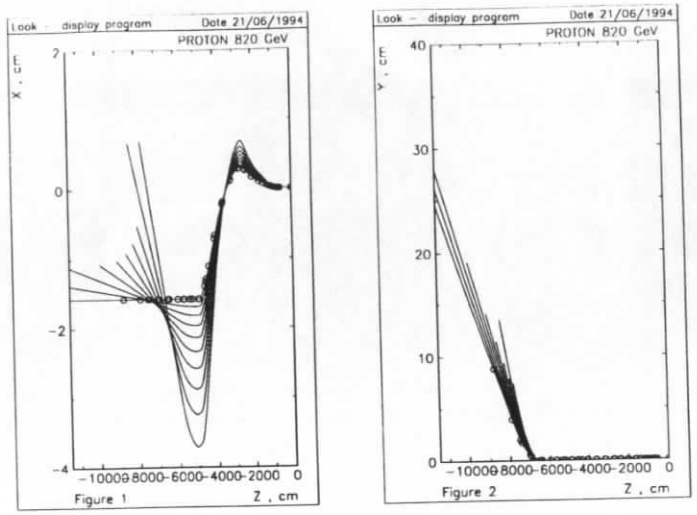

(a) (b)

Figure 10: Horizontal a) and vertical b) spectrometer deflection. The trajectory marked o is the nominal 820 GeV trajectory, the other trajectories are lowered in energy in steps of 50 GeV.

Proton Starting Conditions(Vertex)	
$\epsilon_x = \epsilon_y$	$8.6 \cdot 10^{-9}$m · rad
$\beta_x(0m)$	10m
$\beta_y(0m)$	1m
$\alpha_x(0m)$	0
$\alpha_y(0m)$	0

Table 1: Initial phase ellipse starting values generated

2.2 Proton Trajectory Characteristics

The profile of the circulating beam is described by three quantities, the beam emittance $\epsilon(z)$, the beta function $\beta(z)$ and the inclination $\alpha(z)$ of the phase ellipse in the (x,x') or (y,y') plane for horizontal and vertical coordinates respectively. The z coordinate refers to the direction of the beam axis. The transverse coordinates and slopes are calculated according to

$$x(z) = \sqrt{\epsilon\beta(z)}$$

$$x' = dx/dz = \sqrt{\epsilon\frac{1+\alpha^2(z)}{\beta(z)}}$$

Table 1 shows the starting conditions at the interaction point taken for the simulation of beam protons: The values are taken from HERA optics simulations for 820 GeV protons[9].
In order to check the validity of the beam line simulation, beam envelopes have been generated with a Gaussian profile according to,

$$\sigma(z) = \sqrt{\epsilon\beta(z)}$$

1 σ Beam Profile		
z/m	σ_x/mm	σ_y/mm
0	0.29	0.09
24	0.77	2.22
40	1.60	2.72
44	2.04	2.37
53	3.10	1.40
62	3.12	0.89
81	2.14	0.23
90	1.68	0.34

Table 2: 1σ profiles at various z-positions

In table 2 we show the beam profiles at several z-positions in the forward beam line optics: The beam profile is very similar to events from the HERA machine simulation PETROS [8]. The maximum deviation is in the neighborhood of 1%. The good agreement with the HERA optics calculations gives confidence into the beamline simulation based on the GEANT code.

2.3 Choice of Roman Pot positions

In total five different Roman Pot positions along the beamline are possible. The choice of two positions at 81 and 90 m were based on the following criteria:

- Between the two positions, (81 m and 90 m), there are no magnetic elements; thus, x' and y' can be easily measured.
- Along the beampipe in these regions ample space is available to install Roman Pot mechanics, electronics and shielding.
- The vertical beam profile with $\sigma_y \ll \sigma_x$ is convenient for Roman Pot installation.
- The kinematic acceptance range of these detector combinations (81,90m) enables one to measure $x_p \to 1$.

2.4 Acceptance Range

In the GEANT simulation of the beamline one introduces sensitive detector planes beyond the $\sigma_{x,y}$ beam profiles to register hits in the two pot positions. For the reconstruction one must have a hit in each position in order to determine x', y'. In the following acceptance analysis, we require a coincidence between hits in the 81 and 90 m positions.
Fig. 11 shows the distributions of coincident hits at 81 and 90 m marked by crosses. All hits are contained in the active area covered by the detectors as indicated in the figure. The exact shape of the detectors may be inferred from Fig. 20. In both planes most coincidences are found in the regions immediately above the beam profiles. The simulation of proton trajectories have been made in the proton energy interval $420 < E_p < 820$ GeV and with production angle $0 < \theta < 2$ mrad. The azimuthal angle is generated uniformly. In Table 3 the acceptance for coincidences as a function of the $\sigma_{x,y}$ beam profile cut is shown. It is typically of the order of 10 % for uniformly distributed energies and scattering angles. Furthermore we learn from this

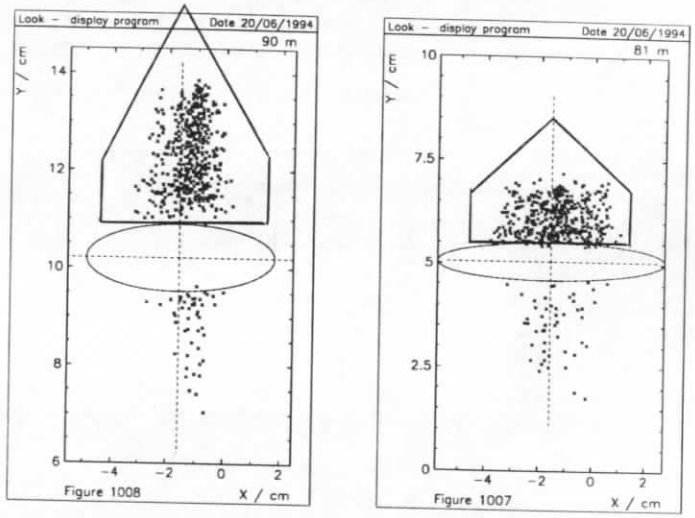

(a) (b)

Figure 11: Coincident hits at 81 and 90 m from protons starting at the interaction vertex. 20σ beam profiles and the active detector areas are indicated.

Coincidence Acceptance			
	Acceptance [%]		
	$\geq 10\sigma$	$\geq 15\sigma$	$\geq 20\sigma$
$(81 \otimes 90\ m)_{all}$	11.9±0.8	10.1±0.7	9.1±0.7
$(81 \otimes 90\ m)_{upperpart}$	9.7±0.7	8.3±0.6	7.3±0.6

Table 3: Coincidence Acceptances for 420$\leq E_p \leq$820 GeV, 0$\leq \theta \leq$ 2 mrad

table that the loss in acceptance is between 17 and 20 % if detectors are installed only above the beam leaving out pots which approach the beam from below.

3 Reconstruction Methods

We compared the GEANT simulation to the transport matrix method. The comparison of the two methods shows that the horizontal and vertical deflections for the nominal momentum (820 GeV) orbits are largely uncoupled. The differences of the two methods is about 10μm maximum which is smaller than the expected spatial resolution. Therefore the linear ansatz for the reconstruction remains largely valid.

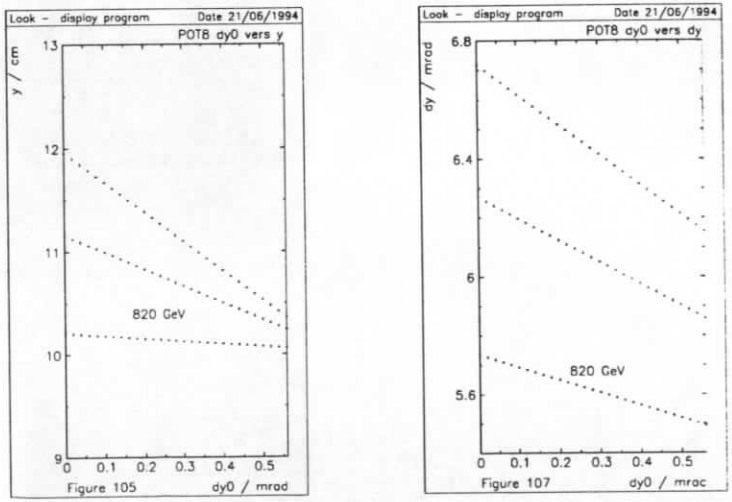

Figure 12: Hit position and projection angle versus the projection angle at the vertex for three different energies of 820,750, and 700 GeV.

In Fig. 12 we show the hit position and projection angle at the tagger position z=90 m for the vertical (y) direction. Both distributions are plotted as functions of the projection angle at the production vertex. From this plot and the corresponding one for the horizontal displacement and deflection angle (ie. x-direction), we can determine x_p, the normalised proton momentum,

Vertex Smearing Parameters	
σ_x/cm	0.033
σ_y/cm	0.010
z_{flat}/cm	50
+ gaussian σ_z/cm	10

Table 4: Vertex Smearing Parameters

as that value of x_p which minimizes the differences in $\Delta x_0^{'}$ and $\Delta y_0^{'}$. These differences are calculated according to the following procedure:
After track reconstruction the space coordinates and slopes of particle trajectories at z=90 m is given by,

$$y_{z=90m} = a(x_p) + b(x_p)\ y_0^{'}$$
$$y_{z=90m}^{'} = c(x_p) + d(x_p)\ y_0^{'}$$

where the coefficients are the slopes and intercepts of the lines seen in Fig. 12. We note that the intercepts and slopes a,b,c and d are to be calculated from the Monte Carlo beam line simulation. It now suffices to solve each of these two equations for $y_0^{'}$. Having done this, we can determine the deviation in $y_0^{'}$ defined as,

$$\Delta y_0^{'} = \frac{[y_{90m} - a(x_p)]}{b(x_p)} - \frac{[y_{90m}^{'} - c(x_p)]}{d(x_p)}$$

The value of x_p is determined as that value which minimizes the difference $\Delta y_0^{'}$. In a similar fashion, the same process is repeated for the horizontal direction, and $\Delta x_0^{'}$ is minimized for yet another independent determination of x_p. The error of x_p is estimated as

$$\Delta x_p = (x_p)_x - (x_p)_y$$

from the two independent determinations. The reconstruction of the proton momentum compared to that simulated is described in the following section.

3.1 Estimation of Resolution under Operating Conditions.

In actual HERA run conditions the vertex is smeared by the proton bunch spread. We show in Table 4 the resultant smearing parameters used in the simulation. Further sources of resolution errors are the finite detector resolution, alignment errors and the multiple scattering in the first detector (ie. 81m position).
In Table 5 we show the expected smearing parameters and their influence on the proton energy resolution. With 100 μm spatial resolution the energy uncertainty is significantly smaller than requested in chapter 1. The vertex resolution could still be improved if one uses the reconstructed event vertex. In current use the vertex smearing is obtained from the global run vertex.
In Fig. 13a and b we plot the difference between reconstructed and generated proton energies

$$\delta = E_{rec} - E_{gen}$$

. Assuming a spatial resolution of 100μm we observe that the momentum resolution is not strictly Gaussian but has larger tails as shown in Fig. 13a, b. In these cases the reconstruction

Resolution		
Hit resolution[μm] σ(y)	σ_E[GeV]	σ_θ [mrad]
0	0.8±0.1	0.012±0.002
100	3.5±0.2	0.013±0.002
200	6.1±0.2	0.018±0.002
400	10.3±0.3	0.025±0.003
800	23.2±1.4	0.043±0.004

Table 5: Resolution after reconstruction

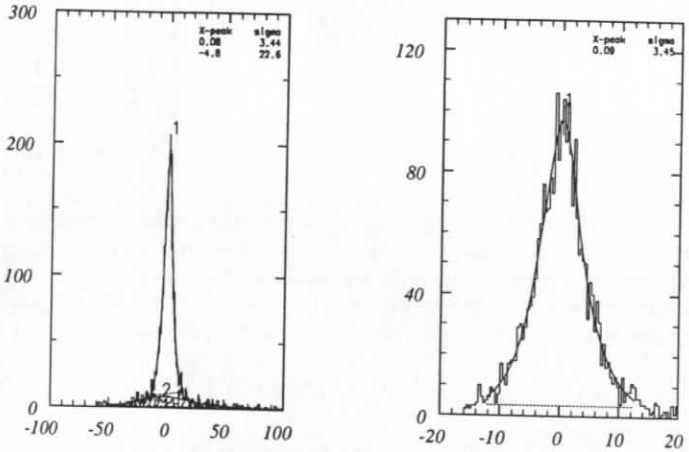

(a) (b)

Figure 13: Energy Resolution for 600$\leq E_p \leq$ 820 GeV assuming a spatial detector resolution of 100 μm (a) all simulated events (b) 2% difference cut applied(see text)

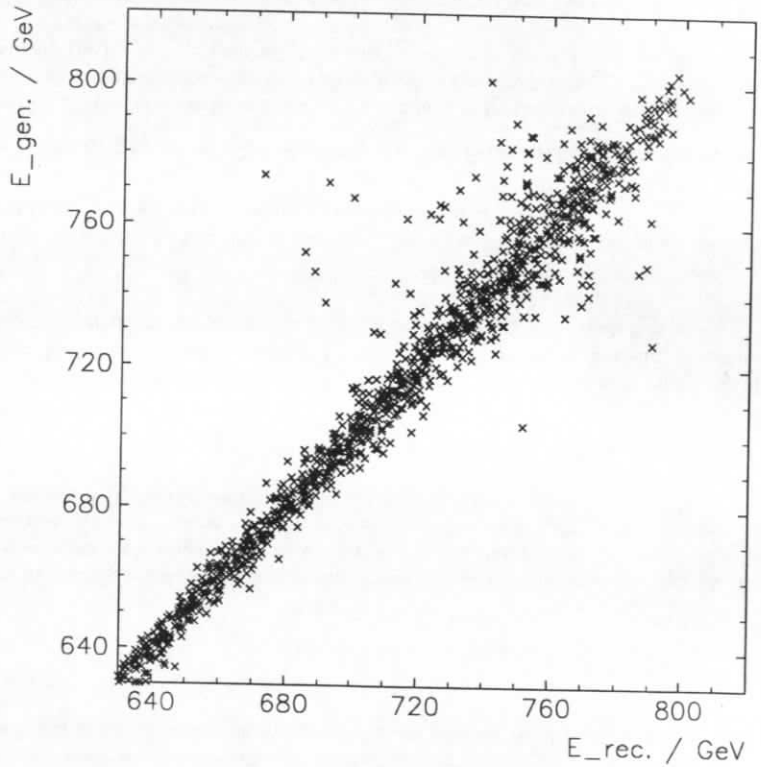

Figure 14: Energy Correlation: Reconst. vs. Generated

method did not converge properly due to large errors intrinsic in the smeared vertex. If the reconstruction error in the vertical (y) coordinate varies by more than 2% by including the horizontal(x) coordinate, the proton trajectory,and hence its momentum, can no longer be determined accurately. This explains the error tails of the distribution shown in Fig. 13a. If we correspondingly plot the energy resolution when the vertical and horizontally determined reconstructed momenta differ by no more than 2%, we obtain Fig. 13b. Finally, in Fig. 14 we show the E_{rec}, E_{gen} correlation.

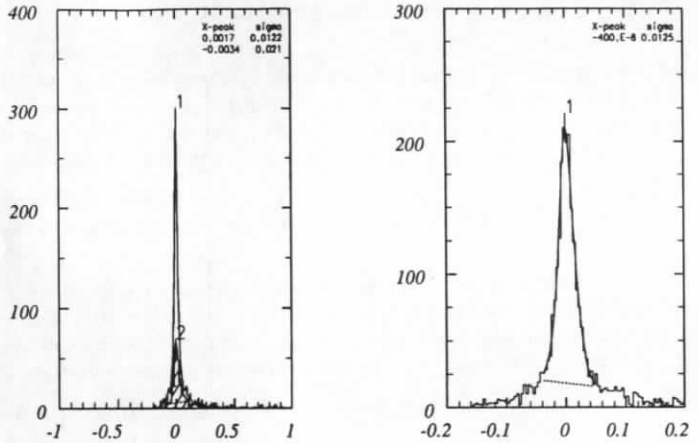

(a) (b)

Figure 15: Angular Resolution for 600$\leq E_p \leq$ 820 GeV: (a)(left) all simulated events (b)(right) 2% difference cut applied(see text)

We note that the energy correlation of Fig. 14 is confined to a narrow band. For energies $E_p >$ 700 GeV the band gets wider due to the unfavourable kinematic configuration for positions 81 and 90 meters. This situation can be improved by adding a further station around 100 m. In Fig. 15 a and b the resulting angular resolution functions are shown. The final energy resolution of the spectrometer as a function of the hit resolution is shown in Table.5.
The expected energy resolution is better than $\sigma_E = 1$ % assuming 100 μm hit resolution and standard smearing parameters for the event vertex. So far no alignment errors have been considered which are expected to be of the order of 50 μm. They will increase the momentum uncertainty to about $\sigma_E = 6$ GeV. This resolution will be sufficient to separate elastic and inelastic processes in most of the kinematic region.

4 Roman Pots.

The Roman Pot principle is sketched in Fig.16. They are vacuum inserts with a plunger vessel at atmospheric pressure to house detector elements. The plunger can be moved into the HERA vacuum pipe with the help of a bellows system and a mechanical gear.

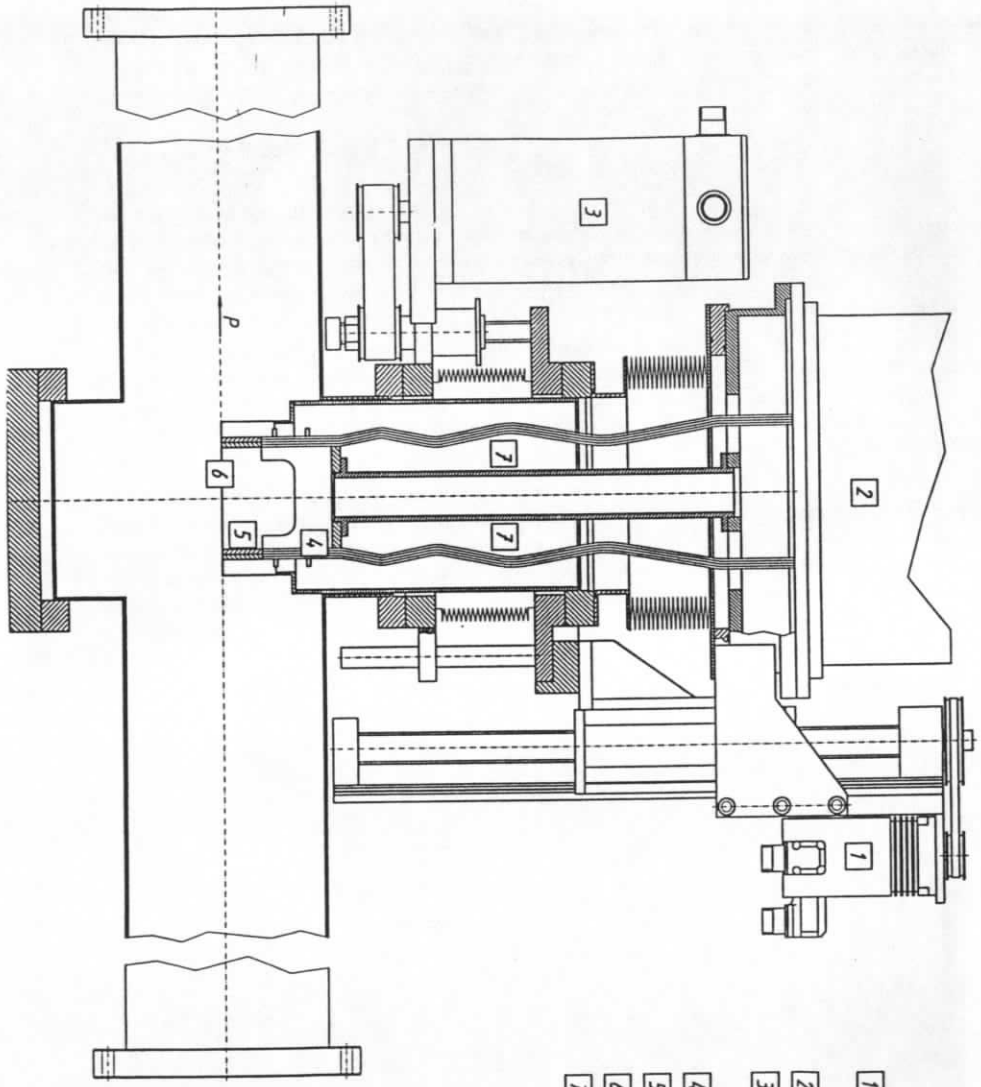

Figure 16

Roman Pots are operated as follows:

1. At injection the Roman Pots are retracted to free the space in the beam pipe, since the full machine aperture is needed to accommodate the low energy proton beam.

2. When stable beam conditions are achieved, the Roman Pots are brought closer to the beam into a position, where they do not limit the beam life time and where single rates in the detector inside the plunger are still tolerable. The latter condition is in general more restrictive than the first one.

3. In order to protect the detectors against sudden beam losses a fast retraction system (v $\approx$ 15 mm/sec) will be installed in addition to the moving gear of the pots. It can be triggered by a beam loss monitor or a pick up station in case of unstable beam conditions. The retraction device can also be used for fine adjustments of the detector positions.

4.1 Mechanical Design

There are two stations foreseen at a position of + 81 m and + 90 m from the H1 interaction point. Fig. 16 shows the vertical section of the 81 m station along the beamline. Each station occupies about 1 m of the beamline and consists of a cross-shaped adapter with CF-flanges at the four ends. One of the two nozzles is blind-flanged for future use, the other (upwards directed) nozzle carries a vacuum tight linear translator, which consists mainly of two flanges being connected by a bellows and guided by 4 rods. The up and down movements are performed by remotely controlled step motors.

4.2 The Plunger Vessel

The plunger vessel is designed to have "windows" and a "bottom" of 0.3 mm thick stainless steel. The windows have to be thin to reduce multiple scattering of the scattered protons. The bottom has to be thin so that the detectors within the plunger vessel may approach the proton beam of HERA as closely as possible, and also to minimise the material placed in the proton beam halo.

The windows and bottom are to be one piece of 0.3 mm stainless steel, originally flat, folded along two straight lines. In this shape it will be welded to the 3 mm thick plunger vessel.

Figure 17 indicates the preparation of the plunger vessel for this welding of the thin windows-and-bottom piece. The edges A and B are straight, but the edge C is curved and so is unsuitable. To replace the edge C with a straight edge D is the purpose of a special piece indicated in the figure. This piece will be welded into the rest of the 3 mm cylinder before the welding of the thin windows-and-bottom piece.

The edges A, B, D must be prepared for the 0.3 mm to 3 mm welding by machining a groove of depth 0.5 mm and width 1.5 mm. An attempt to indicate this groove is made in the figure. Between this groove and the extreme edge is a 1 mm wide recess (not shown in the figure) of depth 0.3 mm, to take the window-and-bottom piece.
The machining and welding of the 3 mm part of the plunger vessels is to be done in the workshops of the School of Physics and Materials, Lancaster University. The final welding of the 0.3 mm windows-and-bottom piece is to be done at DESY.

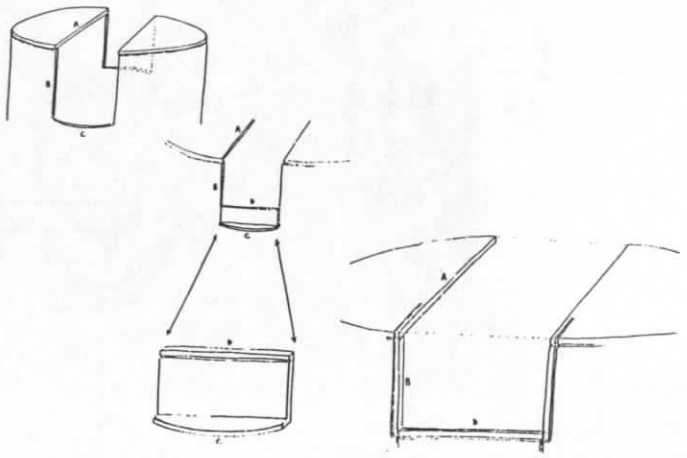

Figure 17: *Welding scheme for the bottom section of the plunger vessel.*

The detector elements and the front end electronics is supported by a second linear moving device consisting of a slide, which is attached to the outer flange of the vacuum linear translator, and a rail carrying a detector support flange. The vertical movement of the detector elements is restricted to 150 mm, the total movement of the detector to 200 mm. The volume inside the plunger vessel is flushed with dry nitrogen, so that in case a window is damaged a contamination of the cold HERA vacuum by humid air is avoided.

Both linear moving devices are actuated by step motors, which are remotely controlled from outside the tunnel. The positions of the plunger vessel and the detectors are determined by the number of motor steps relative to precision micro switches with an accuracy of the order of 5 μm. Moreover the position of the detector can be surveyed by a special displacement measuring system with an electronic readout having a resolution of 2 μm.

All data are transmitted via Ethernet. An emergency function enables a fast retraction of all vessels and detectors in case of e.g. too high background.
In order to establish a reference to the position of the proton beam, a beam pick up monitor with an internal accuracy of 10 μm is being developed together with the DESY group F51 and the DESY machine group.

5 The FPS Detectors.

The detectors have to measure the proton trajectories with an accuracy of about 100 μm, they have to be able to operate with the HERA frequency of 10 MHz and their signals should be adequate for use in the first level fast trigger. Proton momenta are reconstructed from measured space points at 81 and 90 m.

Scintillating fiber detectors as used for tracking in previous experiments, e.g. [10], have been extensively studied by us [11] and have been found to be well suited for the needs of the FPS. They have additional advantages in that the readout electronics can be placed far away from the beam line reducing the risk of a damage by erratic beams. Detector and electronics are separate units and can be replaced separately and the radiation hardness of the fibers of up to 0.1 MGy allows long-term operation close to the proton beam.

We have built several prototype fiber detectors and tested them with light emitting diodes, cosmic particles, in a 5 *GeV* electron test beam at DESY, and in the HERA proton beam line proper. Fast position sensitive photomultipliers (PSPM) [12] were used in the readout. Detailed results can be found in [13] [14].

5.1 General detector design

An overall view of the proposed detector is given in Fig.18. Two subdetectors separated by about 6 *cm* along the beam direction are mounted together with a segmented trigger system to a detector carrier which ensures precise alignment of all components to each other and to the proton beam line. The distance of 6 cm is sufficient for reconstructing vector track elements, it is limited by the diameter of the plunger vessels. Each subdetector has two coordinate planes inclined by $\pm$ 45 degrees with respect to the vertical pot axis. Each coordinate plane consists of five layers of 48 fibers of 1 *mm* diameter positioned parallel within the layers with a pitch of 1.05 *mm*. The layers are staggered by 210 μm, i.e. the pitch divided by the number of layers. In addition the equivalent fibers of both subdetectors are staggered by 105 μm (see Fig.19). The sensitive detector area is shown in Fig.20.

The scintillating fibers with an average length of about 4 *cm* are connected via light guide fibers to the opto-electronic readout system, mounted directly on top of the pots. All fibers of one coordinate of each subdetector are read out by one 64-channel PSPM. For the optical coupling special masks are used which allow precise alignment of the fibers to the PSPM channels. A four-fold multiplexing is applied, i.e. four fibers of one layer, separated by twelve times the pitch, are coupled to the same PSPM channel.

A segmented trigger system is used to resolve the ambiguities resulting from the multiplexing, (Fig.21). For each coordinate two layers of four tiles of 5 *mm* thick scintillator cover the sensitive detector area. The tiles are read out by two 1 *mm* wavelength shifter fibers coupled to light guides which transport the light to 16 photomultipliers on top of the pot. A two-fold coincidence of the photomultiplier signals allows to identify the region were the particle has passed and resolves efficiently the multiplexing ambiguity [14].

5.2 Choice of fibers and light guides

The most important parameter for selecting a suitable type of scintillating fiber is the number of photo electrons produced by minimum ionizing particles but also fiber elasticity and connection possibilities have to be considered.

The number of photo electrons is given by

$$N^{pe} = N_\gamma \int \frac{dE}{dx} \varepsilon_{tr} \varepsilon_q \exp(-l/\lambda)(1-R)^k \, dx$$

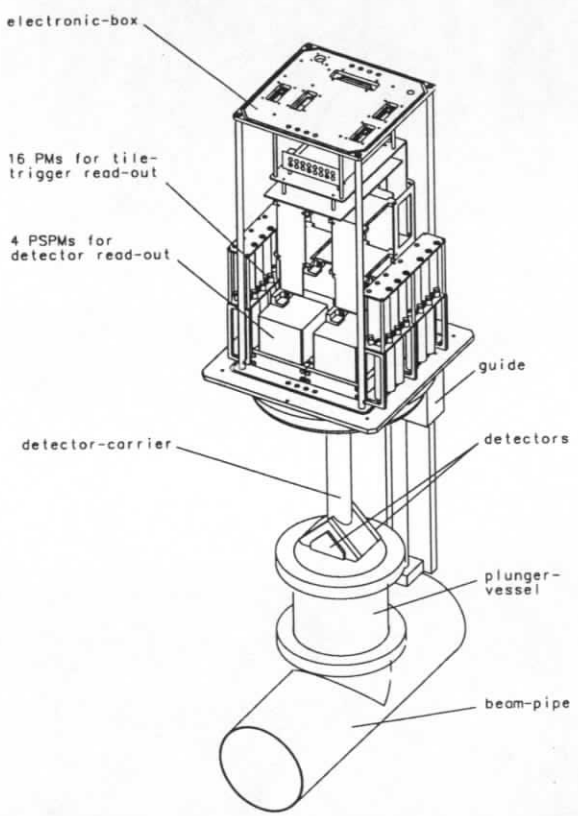

Figure 18: Schematic view of the detector

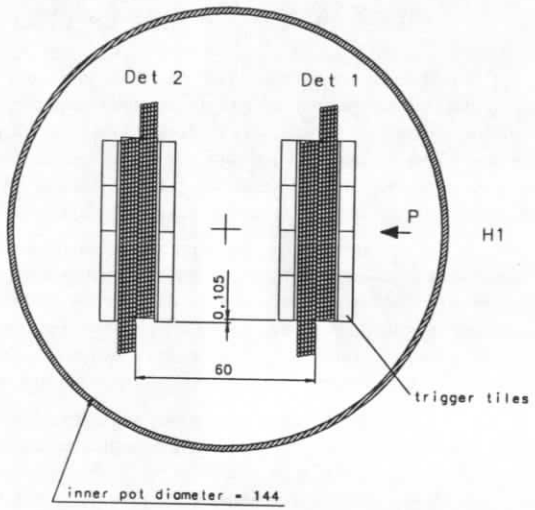

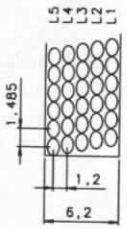

Figure 19: Schematic view of the fiber detector system

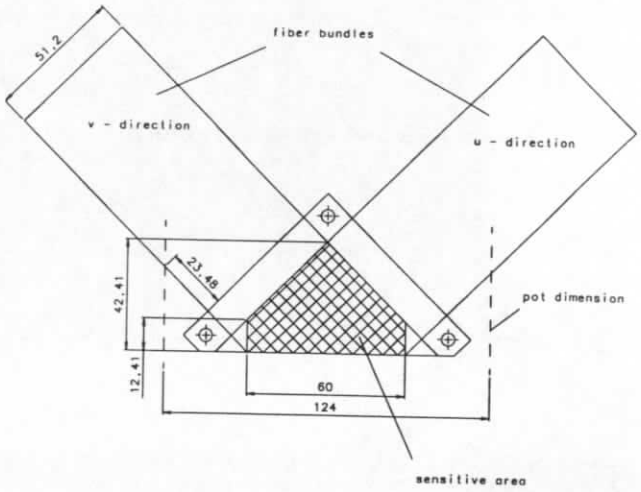

Figure 20: Front view of the fiber detector. The sensitive region is cross-hatched.

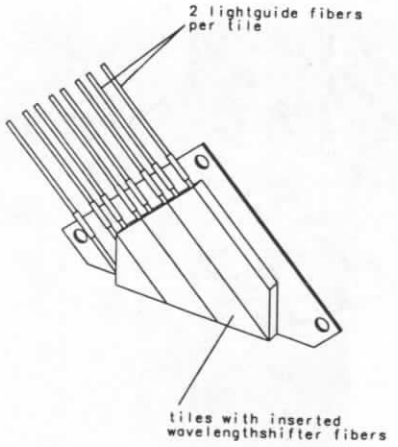

Figure 21: View of a segmented trigger plane

where N_γ is a constant characterizing the scintillating material, dE/dx is the energy loss of the particle, ε_{tr} the light trapping efficiency in one direction, ε_q the quantum efficiency of the optoelectronic read out device, λ the light attenuation in the fiber material and R the single reflection loss at the cladding and k corresponds to the number of reflections.

Assuming:

$$\begin{aligned} N_\gamma &= 10\,\gamma/keV & \varepsilon_{tr} &= 0.03 \\ \frac{dE}{dx} &= 200\,keV/mm & \varepsilon_q &= 0.20 \\ dx &= \frac{2}{\pi}\phi_{fib} & k &= 170 \\ l &= 50\,cm\,, \quad \lambda = 100\,cm, & R &= 5\cdot 10^{-4} \end{aligned}$$

we calculate the number of photo electrons which is well confirmed by measurements with BCF–12 fibers [1] as shown in Table 6. The measurements were performed using a ^{106}Ru source collimated to the fibers.

$\oslash$ [mm]	$< N_{pe}^{calc.} >$	$< N_{pe}^{meas.} >$	$< A^{meas} >$
0.5	2.0	2.0	115
1.0	4.2	4.7	225

Table 6: Average number of photoelectrons, (calculated and measured), and average signal amplitude, (in ADC counts pedestal subtracted), for BCF–12 fibers of 0.5 and 1 *mm* diameter.

The average signal amplitudes in ADC counts for samples of 20 *cm* long circular and square scintillating fibers from different producers are compared in Table 7.

For the coupling of scintillating fibers to optical light guides we investigated two different methods, gluing and thermal splicing. The results are compared in tables 8 and 9 where R is the ratio of the amplitudes for 6.5 *cm* long scintillating fibers coupled to 13.5 *cm* long light guides, to the amplitude obtained for 20 *cm* long scintillating fibers.

Based on these results we decided to use POLHITECH fibers 042-100 of 1 *mm* diameter thermally spliced to the light guides.

5.3 Mechanical detector accuracy

The resolution of the detector depends also on the precision by which the fibers can be positioned, aligned and staggered. Measurements on various test detectors showed that the combined contribution of these geometrical parameters to the resolution can be kept below 20 μm. This is illustrated in figure Fig.22 which shows typical results.

[1] BICRON Corporation, 12345 Kinsman Road, Newbury,Ohio 44065–9677

	$\oslash$ = 0.5 *mm*	$\oslash$ = 1.0 *mm*	sq = 0.5 *mm*	sq = 1.0 *mm*
BCF 12	148	308	129	253
SCSF 38[1]	153		145	
P.H. 042[2]	150	306		
P.H. 046[2]	145	287		
P.H. 048[2]	127	249		

Table 7: Comparison of average signal amplitudes for 20 *cm* long scintillating fibers

[1] KURARAY Co. Ltd, Tokyo, Japan

[2] Pol. hi. tech. S.P. Turanense Km. 44,400–67061 Carsoli (AQ), Italy

R	$\oslash$ = 0.5 *mm*	$\oslash$ = 1.0 *mm*
BCF–12	0.78	0.79
SCSF 38	0.78	-
P.H. 042	0.89	0.97
P.H. 046	0.77	0.79
P.H. 048	0.89	1.07

Table 8: Light output of 6.5 *cm* long scintillating fibers glued to 13.5 *cm* long light guides relative to 20 *cm* long scintillating fibers

	R
BCF–12	0.80
P.H. 042	1.01
P.H. 042[1]	1.12

Table 9: Light output of 6.5*cm* long scintillating fibers thermally spliced to 13.5 *cm* long light guides relative to 20 *cm* long scintillating fibers, $\oslash$ = 1 *mm*

[1] spliced by Pol. hi. tech.

The requirement of about 100 μm accuracy for the measurement of a space point in the FPS detector requires also a high precision of the positioning of the fiber detectors relative to the beam. We use a special alignment plate to position the detectors inside the Roman pots. The overall mechanical accuracy is about 50 μm.

5.4 Opto-electronic readout

We use position sensitive photomultipliers, (PSPM's), for the readout of the fibers. They are available since some years and have been used or are proposed for different types of fiber detectors [11] [12]. They have the advantage of providing large signals which are suited for application in a fast trigger system.

Of the various types of PSPM available we tested the Hamamatsu tubes H4140 and H4139-20 [2]

[2] HAMAMATSU PHOTONICS K.K., Electron Tube Center, 314-5 Shimokanzo, Toyooka village, Iwata-gun, Shizuoka-Ken, 43801, Japan

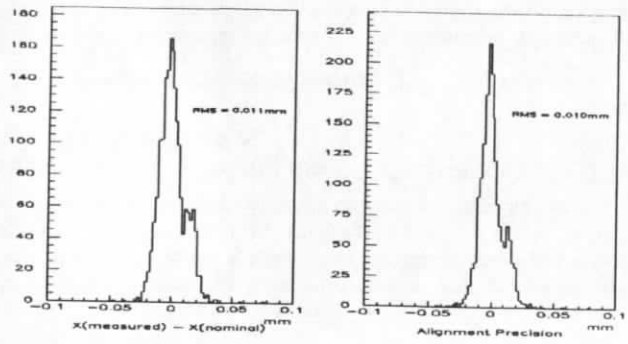

Figure 22: a.) Deviation from the nominal position of 5×100 fibers in four cross sections b.) Deviation of the fibers from a straight line.

and the Philips tube XP1724 [3]. Important parameters as given by the manufacturer are shown in Table 10.
Essential parameters for the functioning of the detector are the internal cross talk and the uniformity of the pixel sensitivity. The best results for these we obtained for the HAMAMATSU tube H4139-20. Results for LED pulses corresponding to about five photoelectrons are shown in Fig.23 averaged over 10000 events. The uniformity of response is in the limits of 2.5 to 1. The detailed analysis of test run data can be found in [14].

5.5 Tile-trigger system

The trigger tiles are made of 5 mm thick scintillator plates of BICRON 408 with embedded wavelength shifter fibers BCF 91A to be read out by photomultipliers XP 1911. The twofold coincidence efficiency of the trigger was measured in the test beam. It is 96 % for minimum ionizing particle tracks [14].

5.6 Detector efficiency and resolution.

With a prototype detector very similar to the one proposed here, (using POLHITECH fibers of similar length and Hamamatsu tubes H4139-20 for readout), we measured a noise corrected single fiber layer efficiency of 62 % [14]. The probability to measure a track point in the detector or in each subdetector separately depends on the number of hits required.

[3]Philips Phototonique, Avenue Roger Roncier, B.P. 520-19106 Brive la Gaillarde, Cedex-France

	XP 1724A	H 4140	H 4139-20
producer	Philips	Hamamatsu	
No. of Pixel	96	256	64
pixel size	2.54 mm	2.54 mm	4.0 Ø pitch 5.08 mm
cross talk	5 %	$\geq$ 50 %	$<$ 2 %
pulse rise time	5 ns	2.7 ns	2.7 ns
dynode stages	10	16	16
gain	10^6 at 1150 V	10^6 at 2500 V	10^6 at 2500 V
qu. eff. 420 nm	$\sim$ 20 %	$\sim$ 20 %	$\sim$ 20 %

Table 10: Technical parameters of position sensitive photomultipliers as provided by the manufacturer

In our test run we used a detector with 16 layers of scintillating fibers. It is split into two subdetectors with eight layers each. Each two consecutive layers are optically multiplexed into a double layer. We found 98 % and 94 % efficiency for detecting a particle if we require hits in at least 3 or 4 of the 8 double layers respectively. The efficiency is 75 % for 3 out of 4 double layers hit in each subdetector.
In this proposal we increase the number of layers per subdetector coordinate to five. Assuming a single layer efficiency as measured in the test beam and demanding to observe at least four out of ten possible fiber hits we achieve 95 % efficiency to record through going tracks. This number is inferred from the plot in Fig.24.
Referring to the results of section 3 it is possible to measure the momentum of crossing particles in 90 % of all cases from one coordinate. The application of the difference criterium when two coordinates are measured reduces this number to about 80 % with an improved resolution.
It could be of an additional advantage to measure a track vector elements in each subdetector of a pot. This allows a further background reduction and provides additional constraints for linking information from both stations with the event vertex. Using reasonable cuts this will be possible for about half the data.

The basic requirement for each of the FPS stations is the measurement of a track point with a precision of about 100 μm. It is however of advantage to measure a track coordinate in each subdetector since this provides additional constraints for the linkage of the information in the two stations and the event vertex.
For a fiber efficiency of 100 % the resolution of the detector depends only on simple geometrical parameters like the diameter of the active fiber core, d, the pitch, D, and the staggering, and can be easily calculated. For the detector which we propose, (d = 0.950 mm, D = 1.050 mm, regular staggering of the 10 planes), we obtain an intrinsic resolution of 28 μm. In reality lower efficiency, cross talk, noise, mechanical imperfections and physics processes like multiple scattering, interactions and delta rays deteriorate this resolution.

To study the influence of these effects a test-run was performed with prototype detectors at

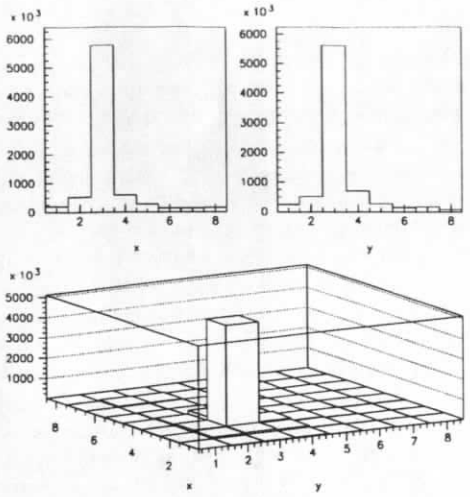

Figure 23: Average amplitude for a single fiber illuminated by LED pulses. (coordinates are in relative anode pixel numbers)

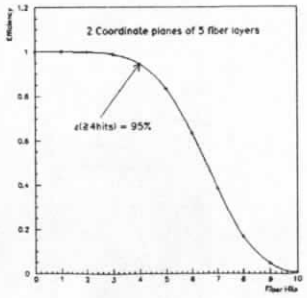

Figure 24: Detection efficiency for reconstructed track points as function of the minimum number of hits.

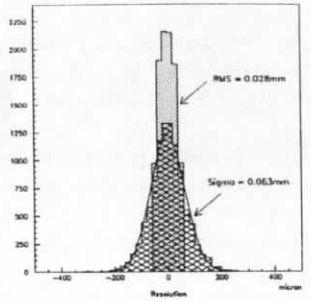

Figure 25: The filled-in histogram shows the intrinsic detector resolution assuming 100 % fiber efficiency.The cross-hatched area represents the resolution for the realistic value of 60 % detection efficiency of a single fiber layer.

a DESY 5 *GeV* electron beam [14]. A silicon microstrip telescope was used for precise track reconstruction. The results on fiber efficiency and PSPM noise behavior were used in a Monte Carlo simulation of the FPS detector configuration. Fig.25 shows the resolution which is 63 μm compared to the intrinsic resolution.

Fig. 26 illustrates the influence of additional effects like interactions and other physical processes during particle crossing, the PSPM cross talk and noise. Although a visible fraction of background coordinates are found by the tracking algorithm the width of the Gaussian peak is only slightly enlarged to 65 μm and the background can easily be removed by the requirement of at least 4 hits per coordinate.

A further deterioration of the resolution is expected from mechanical imperfections in detector construction and alignment which is expected to be less than 50 μm as explained previously. Combining this value with the result of the Monte Carlo simulation yields an overall resolution of less than 100 μm for reconstructed tracks. When reconstructing vector track elements in one station, a resolution of the order of 3 mrad is achieved.

6 Electronics

6.1 Overview

The Roman FPS electronics can be subdivided into three parts:

- The frontend components consisting of preamplifiers and comparators are mounted directly on the detector.

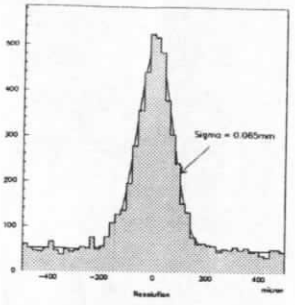

Figure 26: The detector resolution with the presence of physical processes for the crossing particle and PSPM cross talk and noise.

- The conversion and pipelining electronics is located about 10 m away from the detector under the footpath of the HERA tunnel.
- The master controller providing experiment control and data read-out is a VME module residing in a crate in control Room 101.

A block diagram of the first two parts is shown in Fig.E1 for one Pot. The detector is equipped with 4 PSPM's of 64 pixels each. The resulting 256 analog signals are processed at first by charge sensitive preamplifiers with differential outputs to drive the outgoing pulses to the external pipeline crate with sufficient common mode rejection.

The analog information is distributed to 16 pipeline boards of 16 channels each where it is digitized by 6 – bit FADC's. On each board the resulting 96 bits are issued to 12 pipelines of 8 bit width each. The pipeline output registers can be addressed via a 9 – bit address bus and read out via a 8 – bit data bus on the crate backplane.

Additionally each event provides 16 signals of the tile trigger detectors and 4 sum signals of the PSPM's. They are converted to digital informations by fast comparators with remotely controlled threshold. The resulting hit pattern is transferred to the trigger board which is also located in the pipeline crate. Here it is stored in a pipeline and used as input of the trigger processor where the trigger conditions are implemented.

In case of a trigger 256×6 bits = 192 bytes of pixel data and 5 bytes of trigger information are read out by the crate controller. It is connected to the master controller in the control room by means of two bidirectional fiber optic links, one for data exchange and one for control signals.

6.2 Frontend Electronics

Assuming a mean yield of 5 photoelectrons per fiber and an PSPM amplification factor of 10^6, one can expect at the PSPM anode an average charge signal of about 0.8 pC. Therefore a charge sensitive preamplifier with a sensitivity of the order of 100 mV/pC has been foreseen as first step of the signal processing chain followed by a differential driver circuit which is capable to drive the signals via twisted pair cables to the external pipeline crate. According to the connector modularity of the PSPM's the preamplifier boards contain 32 channels which are manufactured in surface mounted technology.

As comparators we use an existing board which already works successfully in the prototype detector. It consists of 16 fast comparators, a part of them being equipped with negative threshold for the tile detector anode signals, the rest of them with positive threshold for the PSPM sum signals.

6.3 Pipeline Board

The pipeline board, a quarter of which is shown schematically in Fig.E2, has been designed to convert and pipeline the informations of 16 PSPM pixels.

The main purpose of the operational amplifier at the FADC input is to sum the following three signal sources:

- the analog pixel information coming from the differential receiver,
- a constant voltage "Low Ref" which shifts the signal level to the sensitive range of the FADC,
- a Test Level which optionally can be added by setting the appropriate Test Bit to test the response of the complete read-out chain on a known input level.

The FADC of type TL5501 has an input range of 1V, a resolution of 6 bits and a maximum conversion rate of 30 MHz. In our application it is clocked by the HERA clock providing the conversion result 96 nsec after conversion start. So the FADC acts as the first stage of the event pipeline.

The FADC output levels are gated to force all bits to zero between two events. This is required by the input stage of the following pipeline device. As shown in Fig.E2, the resulting 24 bits of 4 FADC's are distributed to 3 pipeline registers 8 bits wide in order to save board space and money.

As 32 stage pipeline device we use a special cost effective and highly integrated ASIC chip which has been developed by Hamburg II. 15.000 of them are successfully operated in the H1 Streamer Tube Detector.

Each pipeline output register can be addressed individually via an address bus on the backplane. For reasons of data integrity the read-out of the board address is provided in addition. So the complete address space of one pipeline board is 13 bytes.

6.4 Trigger Board

20 of 24 input lines of the trigger board (see Fig.E3) are occupied by the hit pattern, a digital information consisting of the comparator outputs of 16 tile detectors and 4 PSPM sum signals. First the information is stored in an input register which acts as the first stage of event pipelining like the FADC on the pipeline board.

The register output is connected to the trigger processor, where 8 different trigger conditions implemented by firmware, are checked. This procedure needs only 20 nsec so that the resulting trigger pattern of 8 bits, where each bit represents one trigger decision, can be stored together with the corresponding hit pattern in the pipeline device by the next active clock transition.

The 8 trigger conditions can be activated by means of 8 bits of the trigger mask which is remotely programmable. The final trigger signal then is the logical OR of the masked trigger pattern.

Additionally a facility is provided to measure the arrival time of the first tile detector signal relative to the HERA clock phase. A TDC of 5 nsec resolution is started by the logical OR of all tile detector pulses and stopped by the HERA clock. The resulting 5 bit information is also stored in the event pipeline. So the address space of the trigger board consists of 5 bytes, one for the time measurement, three for the hit pattern and one for the trigger pattern.

6.5 Crate Controller

The main components of the crate controller are six registers which store the necessary configuration parameters, and a finite state machine "Manager" which controls the pipeline register read-out (see Fig.E4).

The configuration registers are programmed via the master controller through the fiber optic link. For verification purposes they can be read back on the same path.

The most important register is the command register where the mode of operation can be selected. The Strobe No. Register defines the number of steps necessary to shift the data of the triggered event to the pipeline output register. By means of the test bit register the test level input of individual channels on each pipeline board can be activated. The mask register provides the 8 bit mask for the different trigger decisions on the trigger board. The comparator thresholds, generated by two DAC's, are issued via the trigger board to the comparator board at the detector.

The read out is clocked by the HERA clock and steered by ENPL (Enable Pipeline), a signal generated by the H1 central trigger controller. If ENPL is true the manager enables the event data to be shifted through the pipelines with HERA clock frequency. If a trigger occur ENPL goes false and the manager stops the pipelines.

The data corresponding to the triggered event are now stored at a certain stage of the pipeline. To read them out the manager first has to transfer them to the end of the pipeline by issuing an appropriate number of strobe pulses STR which is stored in the Strobe No. Register. Then the address counter is implemented and the pipeline output registers are addressed one after another. The data coming from the pipeline boards and the trigger board are transferred directly to the master controller via the fiber optic link.

6.6 Master Controller

As master controller we use the same board which already has been developed for the detector prototype. It mainly consists of an output register and of an input FIFO. Value and type of a data byte which is to be sent to the frontend registers have to be written into the output register. The logic on the board then sequentially sends the data type and the data value via a taxi chip and a fiber optic link to the crate controller where the data is decoded as data destination and the data value is stored in the corresponding register.
Data types and values arriving sequentially at the input port of the board are stored in parallel in the input FIFO of 512 words length. Here the data type distinguishes between trigger data and pixel data. The data transfer rate is 100 MBaud.

On a second bidirectional fiber optic link the signals HCLK and ENPL are sent to the pipeline crate and the trigger signal is received from the crate controller.

6.7 Read-Out Time

For the calculation of the read-out time two parts have to be considered:

a) Transfer of data to the pipeline output (strobe frequency is 5 MHz)
   At most: 32 steps × 0.2 μsec = 6.4 μsec

b) Data read-out (frequency is 5 MHz)
   Pipeline boards: 16 × 13 × 0.2 μsec = 41.6 μsec
   Trigger board 5 × 0.2 μsec = 1.0 μsec

This results in a maximum read-out time of 49 μsec. Since the read-out is performed completely in parallel for each detector the time does not depend on the number of Pots installed.

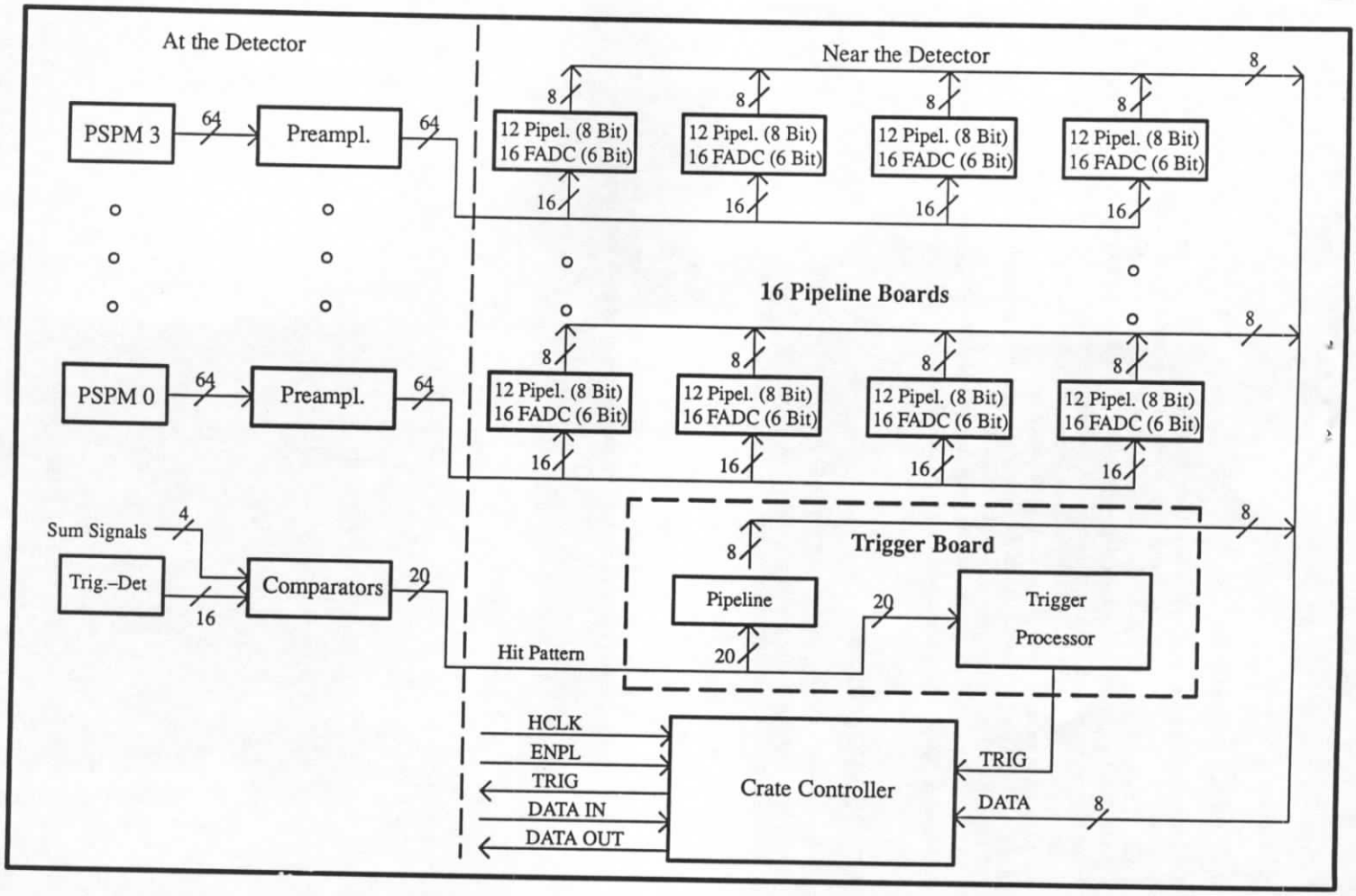

TEB – Hamburg II

Fig. E1: Readout Scheme for one Pot

13.7.94

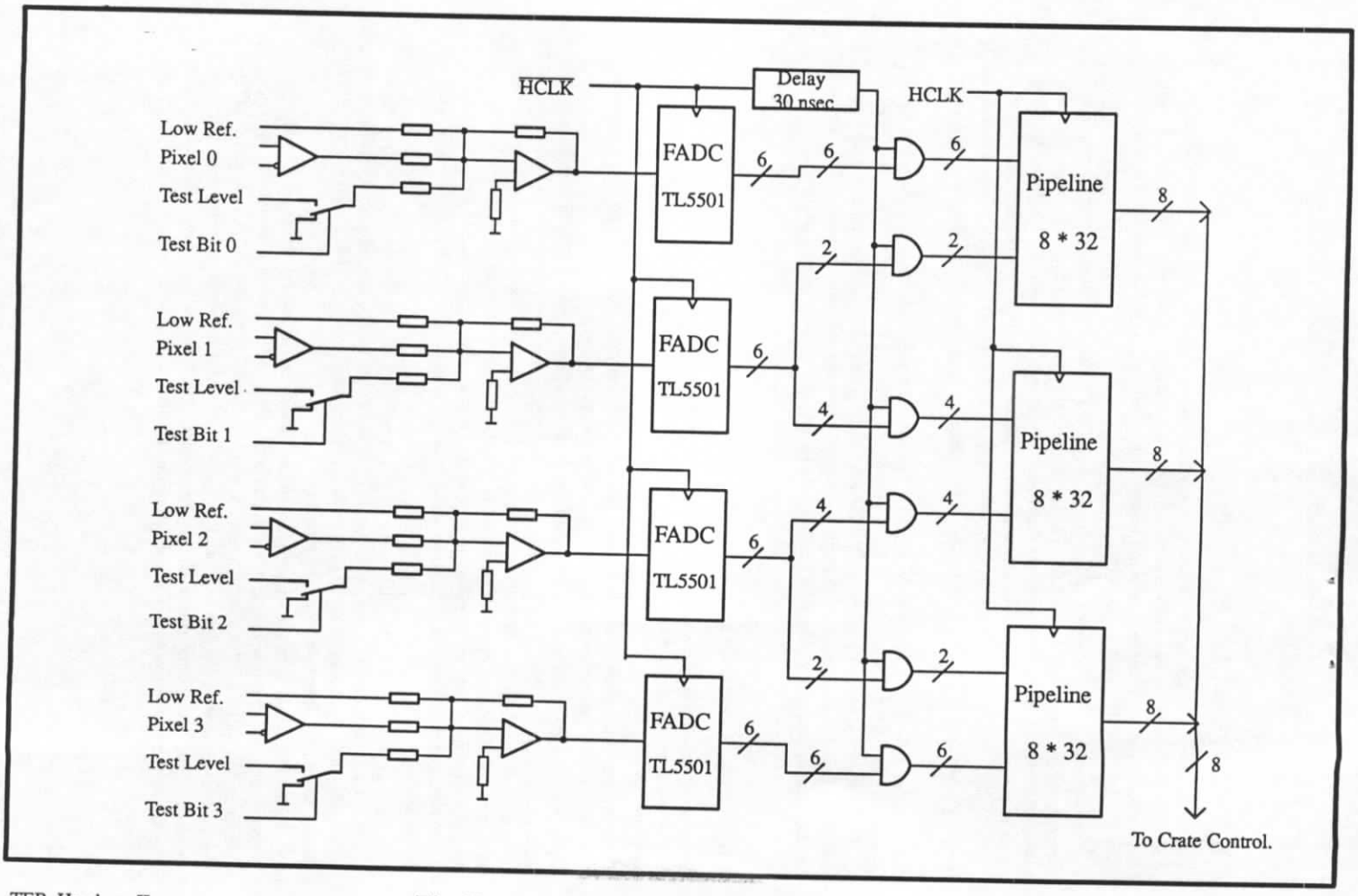

TEB–Hamburg II

Fig. E2: Pipeline Board (4 of 16 Channels)

13.7.94

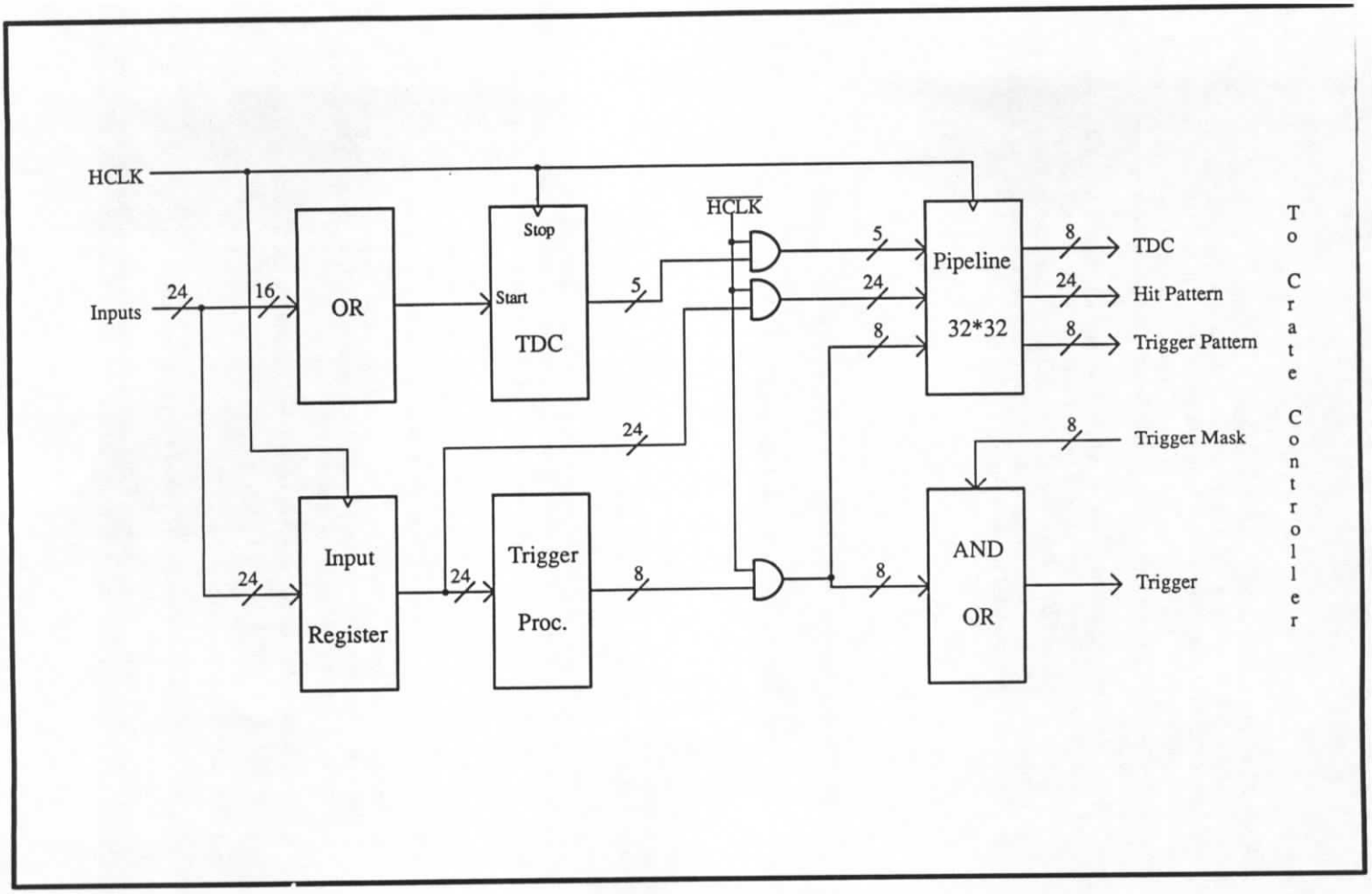

TEB–Hamburg II

Fig.E3: Trigger Board

13.7.94

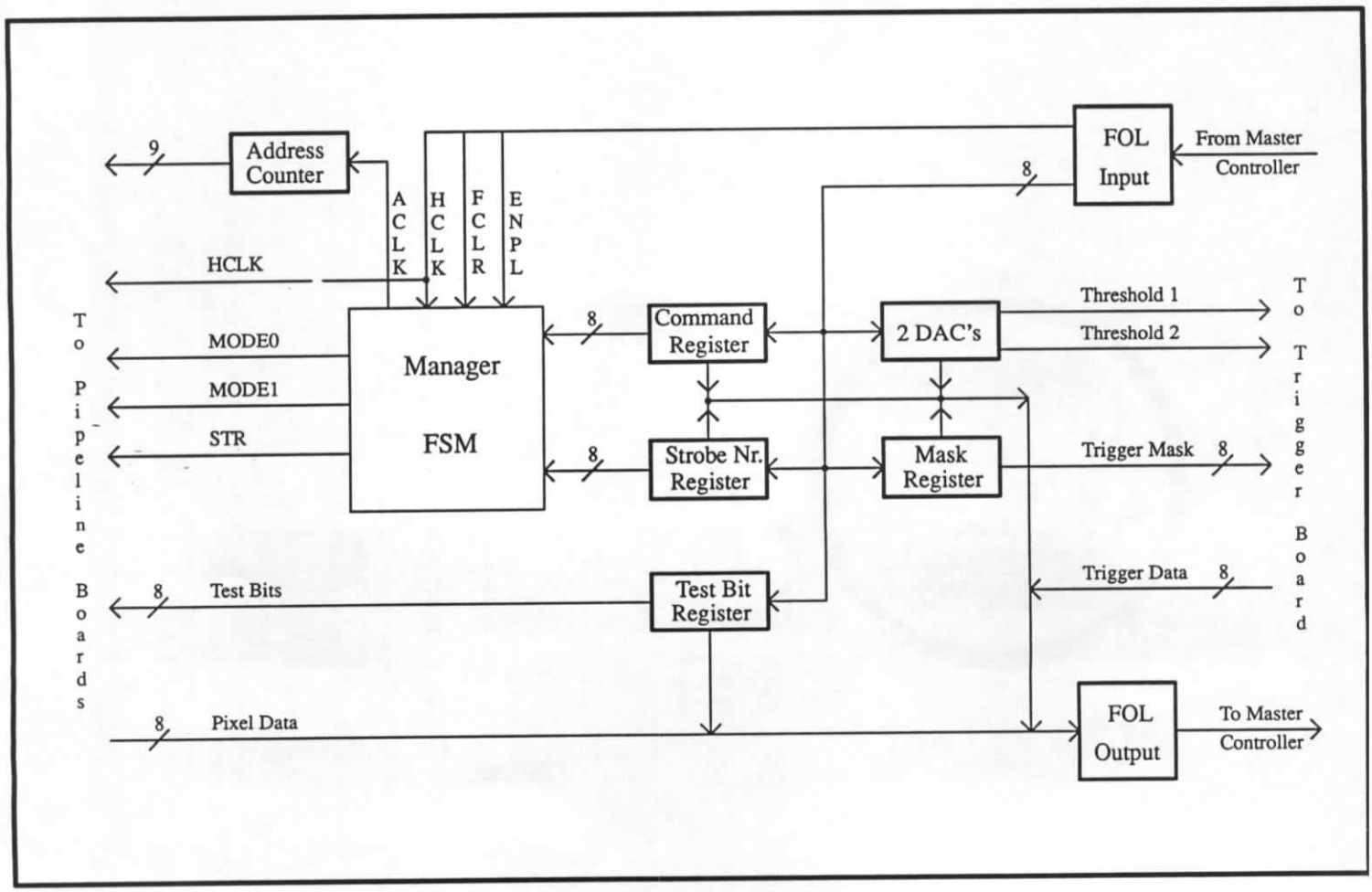

TEB–Hamburg II

Fig.E4: Crate Controller

13.7.94

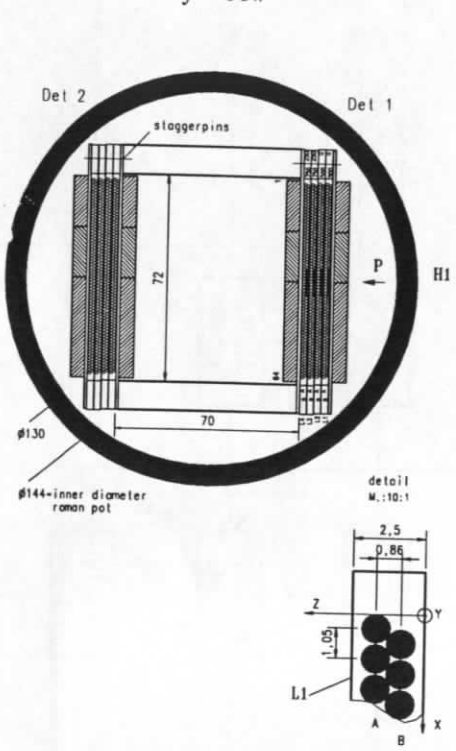

Figure 27: View of the prototype instrumentation of the pot at 81 m. Only the upper part of the hodoscope was actually installed.

7 Test Measurements with Roman Pots at HERA.

In 1994 two Roman Pots at 81 and 90 m are operated during H1 luminosity runs. They are instrumented for test measurements. The 81 m station is equipped with a prototype scintillating fiber hodoscope for one coordinate sandwiched between an array of scintillator tiles for trigger purposes.
The detector arrangement at 81 m is shown in Fig. 27. It consists of 2 planes with 4 double layers of scintillating fibers oriented in the vertical direction so that x - coordinates of traversing particles can be measured. The fibers are read out via two position sensitive photomultipliers (PSPMs), with 64 output channels each. The hodoscopes are sandwiched between two planes of trigger counters consisting of three trigger tiles with wavelength shifter and fiber read out connected to conventional photomultipliers. The instrumentation at 90 m is simpler. It has trigger tiles only.
A stand alone trigger signal is formed with the help of the 12 trigger tiles in each pot. In order

to relate hits, which are registered in the two stations, to H1 triggers, the scintillator signals are fed into the H1 datastream via a GPTP (General Purpose Trigger Pipe) card. For this purpose the flight path between 81 and 90 m is compensated by a delay cable and the signals are synchronized with the HERA clock. With each H1 event the signals of 9 consecutive bunch crossings are read out, centered around the trigger bunch. The bit pattern is stored in the VETE bank.
In addition to the H1 triggered read out an independent read out chain is installed which is based on the local tile trigger. Both systems work in parallel. They are sketched in Fig. 28. The local branch reads all fiber information digitised by FADC's and all scintillator hits. In order to relate local triggers to H1 triggers in an off line analysis the status bits of HERA revolution counters are appended to the events.
The aims of the 1994 tests are:

- Measure rates induced by the proton and the electron beams and to determine their variation with the distance to the beam.
- Look for correlations between events observed in the H1 detector and signals in the FPS.
- Derive estimates for the expected trigger rates for different trigger conditions.

7.1 Electron Beam Related Background

7.1.1 Observations

Electron beam related background may be caused by spent electrons resulting in energetic shower particles or by synchrotron radiation from the arcs with a critical energy of about 86 keV. It is observed that counting rate in the scintillators at 90 m is not affected by the circulating electron beam. At 81 m a strong influence is seen.

- Before any shielding was installed the counting rates for individual scintillators were in the range of 100 to 1000 kHz at electron currents of 20 mA with the scintillators 20 cm away from the proton beam. These rates have to be compared with a noise ranging between 500 and 1000 Hz.
- The rate of the electron related signals is proportional to the electron current.
- The observed rate in the scintillators is proportional to their respective areas.
- The rate in the tiles varies with their vertical distance from the beam (see Figure 29). When the tiles were shadowed by a flange of the plunger vessel at a reading of about 70 mm, the counting rate dropped by a factor of 3.
- The application of 2 mm lead shielding around the complete installation reduced the rate by roughly a factor of 3.

From these observations we conclude:

- That the electron related signals are caused by synchrotron radiation.
- That the radiation is hard, dominated by photons with energies above 50 keV.

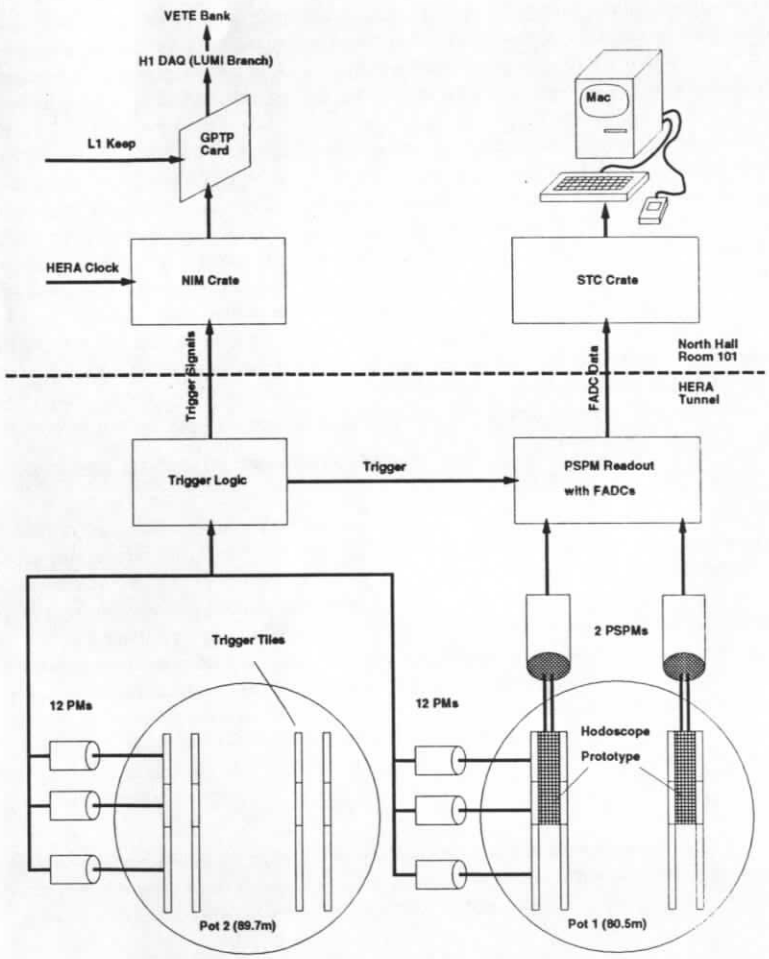

Figure 28: Sketch of the readout electronics used for the trigger tile readout via the H1 DAQ.

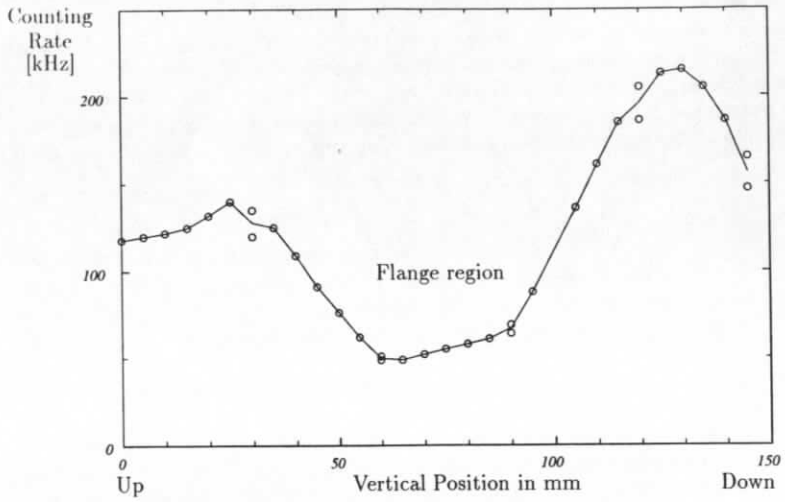

Figure 29: Single rates in one trigger tile at 81 m as a function of the vertical position. The 150 mm position corresponds to a distance of 50 mm from the closed orbit.

The synchrotron radiation background was successfully suppressed by eliminating the source with lead walls between the electron and the proton ring. After the shielding operation the single rates at 81 and 90 m where about equal of the order of 1 KHz and no significant influence of the electron beam was observed.

7.2 Proton Induced Signals.

The proton induced rates in the scintillator tiles are summarised in Table 7.2. The single rates 50 mm away from the circulating beam are typically a few kHz with coincidence rates of some 100 Hz. Moving the detectors towards the proton beam only a moderate increase of rates is observed as long as the pots remain within the shadow cast by the HERA collimators in the straight section West. Leaving the shadow leads to a dramatic increase because the bottom plates of the plunger vessels start scraping the beam. Good operating conditions are met between 0.05 and 0.1 mm away from the sharp edge of the collimator shadow. This distance corresponds to about 15 σ or 3.4 mm distance to the nominal beam. rates are then higher by about a factor of two compared with the retracted position.
Signals induced by the proton beam may be due to particles from e - p interactions which are also observed in the H1 detector, or to interactions that are not triggered by H1 either because the secondaries of a genuine e - p interaction did not reach the H1 trigger elements or it occurred between the detector and the FPS in the case of beam–gas or beam–wall interactions. The two classes of events may be distinguished by their timing properties. Events which are related to H1 triggers will appear in one particular time bin while those not related to H1 triggers will

	81 m		90 m	
	up	down	up	down
Single rates	1–9 kHz	2–9 kHz	2–7 kHz	3–8 kHz
3/4 coincidence	250 Hz	1000 Hz	1000 Hz	3000 Hz
4/4 coincidence	130 kz	500 Hz	700 Hz	2000 Hz

Table 11: Typical counting rates of single scintillators, and for 3–out–of–4 and 4–out–of–4 coincidences in one row for proton currents of 40 mA and positron currents of 15 mA. "Up" and "Down" refers to the pot positions 50 mm and 3 mm from the beam axis.

have a uniform distribution in time.
If we divide the 12 trigger tiles in a station into 3 rows each 4 counters deep we may study coincidence rates of various levels as a function of the read out time slices shown in Fig. 30 for pot positions 15 σ away from the nominal orbit. The top row of the figure shows the two, three and fourfold conicidences in rows a, b and c at 81 m, while the lower row corresponds to the 90 m position. In all cases a clear enhancement at the time bin 0 is observed, which corresponds to the time of the H1 trigger. The neighbouring bins have a uniform distribution corresponding to a background level of less than 5 %.
These observations prove that at a distance of 3.4 mm from the circulating beam tracks can be registered at a low background level of a few %. The particles registered in the Roman Pots are clearely realted to events triggered by H1.

7.3 First fiber detector measurements

The readout system for the fiber hodoscope at the 81 m station employs an electronics system based on MX4 boards, which have been used in lab tests but are different from the scheme described in chapter 6. Therefore special timing and threshold adjustments had to be made.
At positions around 3.5 mm from the circulating proton beam several thousand triggers have been recorded in different runs demanding four-fold coincidences from the trigger tiles which sandwich the fiber detector. One additional run has been taken where eight-fold coincidences of all tiles of both pot 1 and 2 have been selected. Clear signals correlated to proton bunches were observed in both cases. In Fig 31 a and b we show the trigger delay with respect to the opening time of the active window of the readout electronics for pot 1 and 2 respectively. The peaks at 30 *nsec* in pot 1 and 20-25 *nsec* in pot 2 correspond to the proper time behaviour of throughgoing protons. Therefore these triggers can easily be separated from the background at other times.
Demanding to observe at least three out of four possible hits for a crossing particle in the double layers of subdetectors 1 and 2 we are able to calculate track gradients for a clean data sample. The result is shown in Fig. 32 As expected we observe a strong peak at very small track angles due to high energetic protons. The background from any type of additional interactions is small. This becomes even more clear by an eye scan of a larger event sample. A typical event as seen at the online data display is given in Fig. 33
The very first fiber detector results give already a positive answer to the main question of the prototype test. The detector is able to operate under HERA conditions at a considerable low

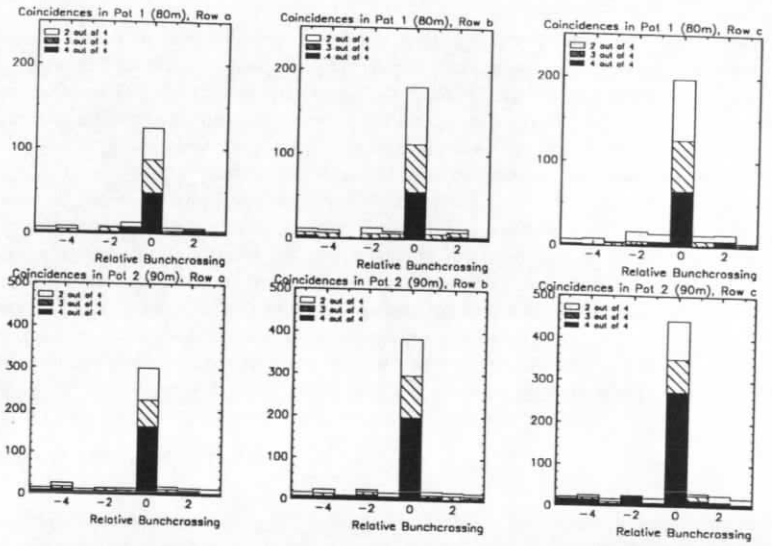

Figure 30: Coincidence rates of various levels in time slices around the H1 trigger signal. The top three histograms refer to the 81 m station with the three rows of trigger tiles. The lower histograms are taken at 90 m. E_p=820 GeV, I_p=36 mA, E_e=27 GeV, I_e=19 mA.

background rate. Now a fine tuning of hardware and software parameters will improve the data quality further.
Selecting clear track candidates a first estimation of the detector efficiency has been made. For this purpose a track has been defined by at least three overlapping hits in one subdetector and two in the other one. One double layer has been excluded from this procedure and its efficiency has been calculated dividing the number of hits found at the right track position by the number of predicted ones. Background hits are subtracted afterwards comparing with a region outside the track corridor.
The results are presented in figs. 34 a and b for all four double layers of both subdetectors. An average efficiency of about 75% and 70% is found for subdetectors 1 and 2 with only small variations between the double layers. This result confirmes the testrun measurements [14] and proves the design of the full scale detector.

7.4 First events

With the scintillators close to the circulating proton beam, events were selected from DST tapes which had fourfold tile coincidences in both stations. This may be interpreted as a signal from an energetic forward going proton indicating that the event may be of diffractive nature. In Fig. 35 a tagged photoproduction event is shown. Events of this type clearly show the physics potential of the forward proton spectrometer. In the H1 detector secondary particles are observed down to small forward angles and the event would not be classified as a rapidity gap event, which up til now is used as a creterium to classify diffractive like event topologies.

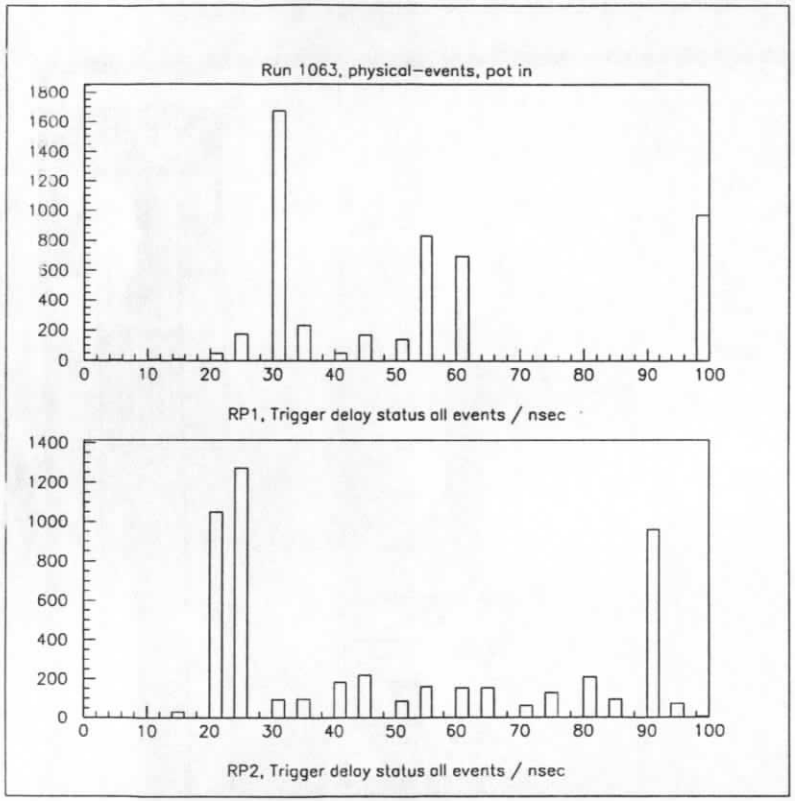

Figure 31: Trigger delay with respect to the opening of the active window of the readout electronics for pots 1 and 2

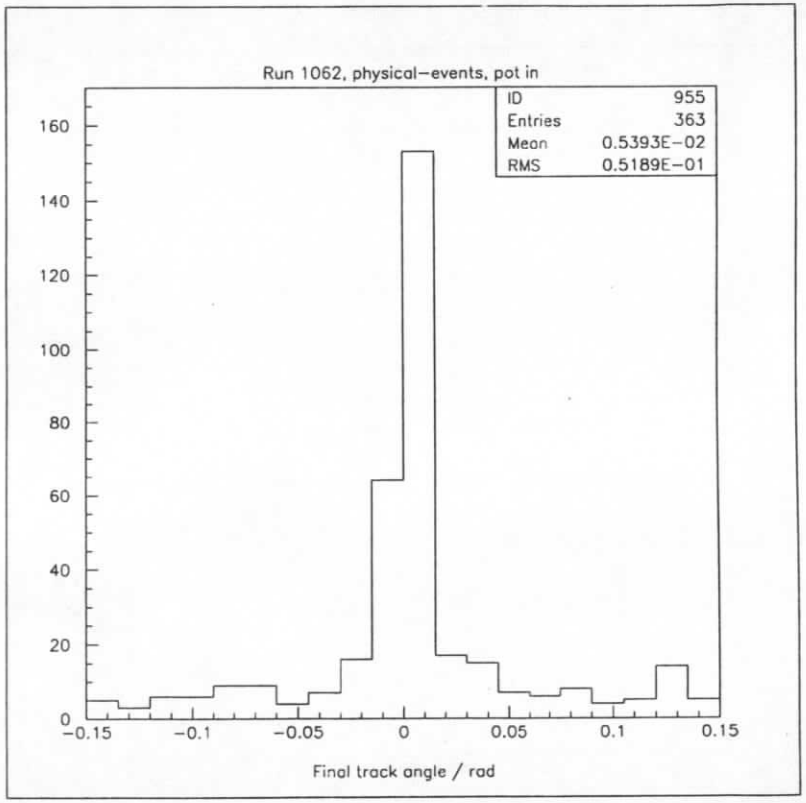

Figure 32: Track angle of particles crossing the fiber detector

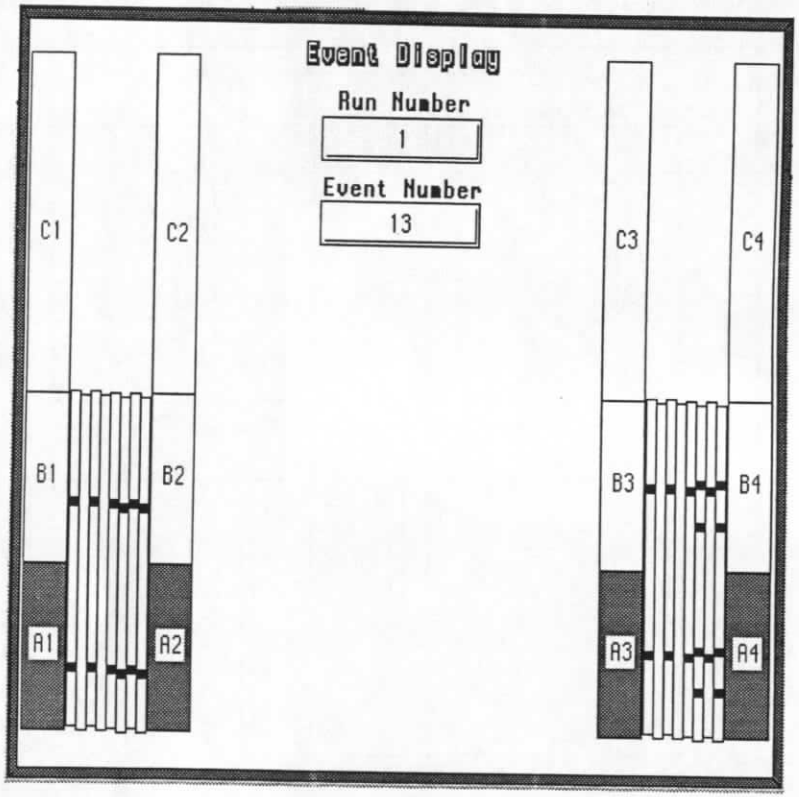

Figure 33: Response of the fiber detector to a crossing particle as shown by the online display.

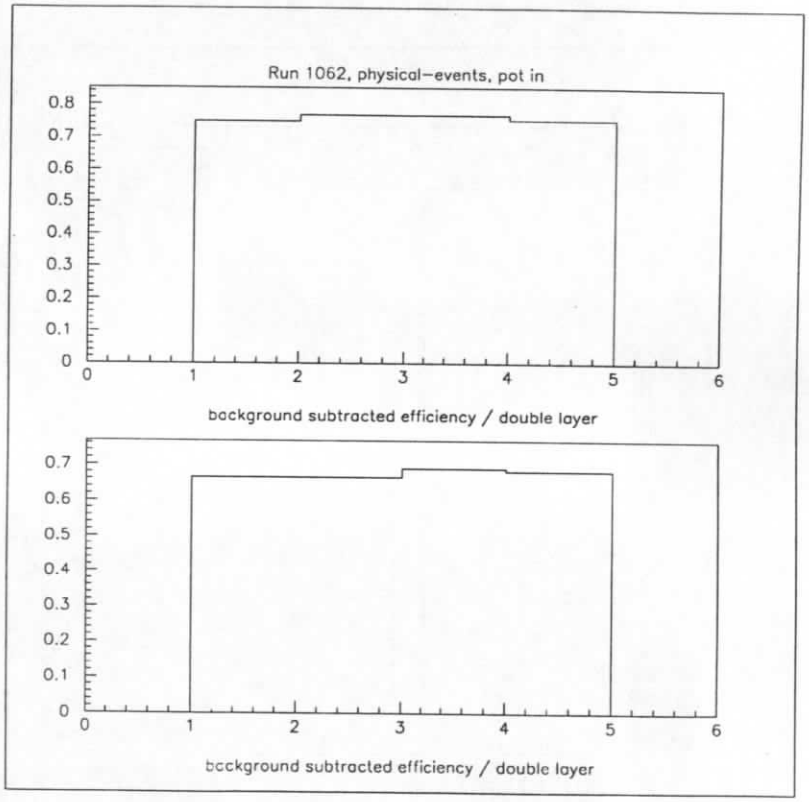

Figure 34: Background subtracted double layer efficiency to record a hit from a crossing particle (for subdetectors 1 and 2)

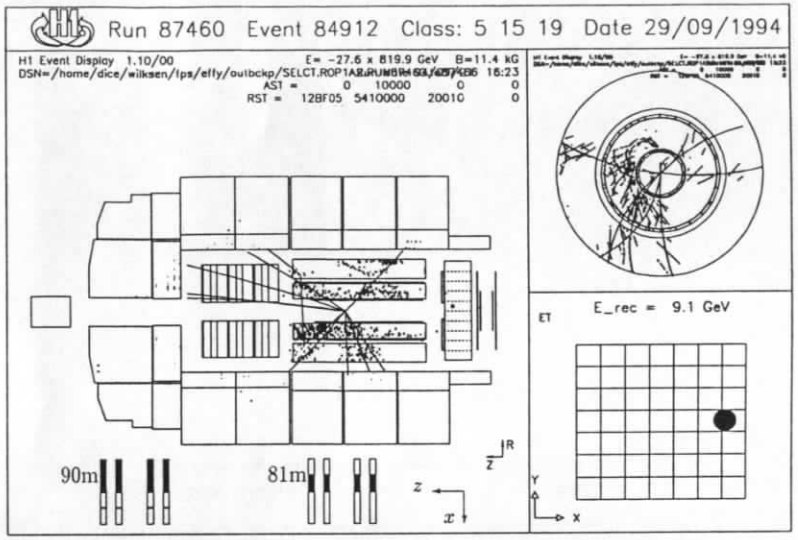

Figure 35: A photoproduction event with an electron detected in the electron tagger. This events was taken in a run where the pots were close to the beam.

From Monte Carlo studies we expect a large fraction of diffractive events to have a rapidity gap above four units in pseudorapidity. These reactions can only be identified with the help of very forward detectors. The signal in the Roman Pots furthermore tells us that the incident proton has surviwed and the event of Fig. 35 thus being a good candidate for a photoproduction reaction with Pomeron exchange.

8 Conclusion.

An upgrade for the H1 detector is proposed by adding a forward proton spectrometer with two detector stations at 81 and 90 m downstream the interaction point. The Roman Pot technique will be employed to bring scintillating fiber hodoscopes and trigger counters close to the circulating proton beam. Space points and vector track elements will be measured at the two stations with an accuracy which is sufficient to achieve a momentum resolution of 1% and to suppress background tracks from beam gas and beam wall interactions. In test measurements the technique of operating scintillating fiber hodoscopes has been proven to fulfill all requirements for an operation at the HERA collider. First results from rate measurements with prototype detectors during the 1994 physics runs show that the background conditions are favourable and a correlation between events triggered by the H1 main detector and particles, which where recorded in the Roman Pots, can be established.
Based on the positive outcome of previous tests we are certain that a forward proton spectrometer for H1 can be built and can be put into operation for the physics runs of 1995.

9 Cost estimates, Responsibilities, Time table.

Cost – Estimates

Items	Prices (kDM)
8 Positionsensitive Multipliers	160
Hodoscopes of Scintillating Fibers	50
Electronics	70
Roman – Pots, Mechanics	70
Slow Electronics, Trigger –counters	30
Precision beam monitor	50
Installation, Alignment	40
Tools, Laboratory – Equipment	20
Total Costs	**490**

Responsibilities

Parts	Institutions
Design and Construction of the Roman Pots	DESY, Lancaster
Construction of the Fiber – Detectors	Zeuthen
Optoelectronics, Tests Manufacturing, Final Assembly	Brüssel, DESY Hamburg II, Kiel, Zeuthen
Installation	DESY
Front – End – and Readout – Electronics	Hamburg II
Data – Acquisition	DESY, Hamburg II, Kiel Lebedev, Zeuthen

Timetable

Items	Timeschedule
Test of Prototype – Detector	Run – Period 1994
Manufacturing of the Detectorhodoscopes and Electronics	up to February 1995
Assembly	During the Shutdown 94/95

References

[1] M. Derrick et al. ZEUS collaboration Phys. Lett. B315 (1993) 481
H1 collaboration, paper submitted to Nucl. Phys. B.

[2] G. Alberi, G. Goggi Phys.Rep. 74(1981) 1
K. Goulianos Phys. Rep. 101(1983) 169

[3] G. Ingelman, P.E. Schlein, Phys. Rev. Lett. 152B (1985) 256
A. Donnachie, P.V. Landshoff, Nucl. Phys. B303 (1988) 634

[4] H. Mahlke, Diploma Thesis, Hannover 1994 (unpublished)

[5] P. Bruni, G. Ingelman, DESY 93-187

[6] The ZEUS Detector – Technical Proposal
The ZEUS Detector – Status Report 1993

[7] F.G. de Bilio: GEANT3 User's Guide, CERN DD/EE/84-01, May 1986.

[8] R. Brinkmann, B. Holzer: private communication, Actual Properties in the Straight Section of the Proton Ring, Nov. 1992.

[9] R. Brinkmann: HERA Lattice and Optics Design, Bad Lauterbach, 1992(proceedings).

[10] UA2, C.N. Booth et al., NIM A273 (1988) 826
UA2, A.R. Weidberg et al., NIM A283 (1989) 646

[11] J. Bähr et al., NIM A 324 (1993) 145
J. Bähr et al., NIM A 330 (1993) 103.

[12] J. Bähr et al., DESY preprint DESY 93-201 and
proceedings of the "International workshop on scintillating
fiber detectors SCIFI-93", Notre Dame 1993

[13] J. Bähr et al., proceedings of the "International workshop on position
sensitive detectors", London 1993
J. Bähr et al., DESY preprint DESY 93-200 and
proceedings of the "International workshop on
scintillating fiber detectors SCIFI-93", Notre Dame 1993

[14] J. Bähr et al., DESY preprint DESY 94 – 130